

ALMA + VLT observations of a Damped Lyman- α absorbing galaxy: Massive, wide CO emission, gas-rich but with very low SFR ^{*}

P. Møller¹†, L. Christensen², M. A. Zwaan¹, N. Kanekar³, J. X. Prochaska⁴, N. H. P. Rhodin², M. Dessauges-Zavadsky⁵, J. P. U. Fynbo², M. Neeleman⁴, T. Zafar⁶

¹European Southern Observatory, Karl-Schwarzschildstrasse 2, 85748 Garching bei München, Germany

²Dark Cosmology Centre, Niels Bohr Institute, Copenhagen University, Juliane Maries Vej 30, 2100 Copenhagen O, Denmark

³National Centre for Radio Astrophysics, TIFR, Post Bag 3, Ganeshkhind, Pune 411 007, India

⁴University of California Observatories/Lick Observatory, University of California, Santa Cruz, CA 95064, USA

⁵Observatoire de Genève, Université de Genève, 51 Ch. des Maillettes, 1290 Sauverny, Switzerland

⁶Australian Astronomical Observatory, PO Box 915, North Ryde, NSW 1670, Australia

13 March 2022

ABSTRACT

We are undertaking an ALMA survey of molecular gas in galaxies selected for their strong HI absorption, so-called DLA/sub-DLA galaxies. Here we report CO(2-1) detection from a DLA galaxy at $z = 0.716$. We also present optical and near-infrared spectra of the galaxy revealing [OII], H α and [NII] emission lines shifted by ~ 170 km s⁻¹ relative to the DLA, and providing an oxygen abundance 3.2 times solar, similar to the absorption metallicity. We report low unobscured SFR $\sim 1 M_{\odot}$ yr⁻¹ given the large reservoir of molecular gas, and also modest obscured SFR = $4.5^{+4.4}_{-2.6} M_{\odot}$ yr⁻¹ based on far-IR and sub-mm data. We determine mass components of the galaxy: $\log[M_{*}/M_{\odot}] = 10.80^{+0.07}_{-0.14}$, $\log[M_{\text{mol-gas}}/M_{\odot}] = 10.37 \pm 0.04$, and $\log[M_{\text{dust}}/M_{\odot}] = 8.45^{+0.10}_{-0.30}$. Surprisingly, this HI absorption-selected galaxy has no equivalent objects in CO surveys of flux-selected samples. The galaxy falls off current scaling relations for the SFR to molecular gas mass and CO Tully-Fisher relation. Detailed comparison of kinematical components of the absorbing, ionized and molecular gas, combined with their spatial distribution, suggests that part of the CO gas is both kinematically and spatially de-coupled from the main galaxy. It is thus possible that a major star burst in the past could explain the wide CO profile as well as the low SFR. Support for this also comes from the SED favouring an instantaneous burst of age ≈ 0.5 Gyr. Our survey will establish whether flux-selected surveys of molecular gas are missing a key stage in the evolution of galaxies and their conversion of gas to stars.

Key words: galaxies: abundances – galaxies: formation – galaxies: evolution – galaxies: high-redshift – galaxies: ISM

1 INTRODUCTION

Since the discovery of the first damped Ly α absorber (DLA) at high redshift ($z = 2.31$; Lowrance et al. 1972) almost half a century ago, the nature of the objects causing this absorption has been an important open problem in galaxy evolution. A wide range of suggestions, including large galaxy disks, gas-rich dwarf galaxies, circumgalactic gas, tidally-stripped gas in merger events, and starburst-driven outflows, have been put forward to explain var-

ious properties of the absorbers (e.g. Prochaska & Wolfe 1997; Haehnelt et al. 1998; Nulsen et al. 1998; Fynbo et al. 1999; Schaye 2001). However, no single galaxy class has so far been able to explain all the properties of the known DLA sample. Of course, the absorber sample is likely to be drawn from the full galaxy population at any redshift and will thus certainly contain galaxies of different types.

The main limitation in addressing the question of the nature of the DLA host galaxies has been simply the fact that the bulk of our information on DLAs stems from absorption studies, which trace only a pencil beam through the host galaxy. While such studies have provided detailed information on the HI column density distribution function, the elemental abundances, the gas-phase metallicities and dust depletions, the absorption kinematics, the spin temperatures, and the molecular gas fractions in

* Based on observations at ESO; Program IDs: 095.A-0890(A)(FORS), 079.A-0673(A)(Sinfoni), 274.A-5030(A)(UVES); 2013.1.01178.S (ALMA). Herschel is an ESA space observatory with science instruments provided by European-led Principal Investigator consortia and with important participation from NASA.

† E-mail: pmoller@eso.org

DLAs at all redshifts (e.g. Prochaska & Wolfe 1997; Pettini et al. 1997; Storrie-Lombardi & Wolfe 2000; Kanekar & Chengalur 2003; Prochaska et al. 2003; Kulkarni et al. 2005; Prochaska et al. 2005; Ledoux et al. 2006; Noterdaeme et al. 2008; Rafelski et al. 2012; Noterdaeme et al. 2012b; Kanekar et al. 2014), they have offered limited insight into the link to emission selected samples. Unfortunately, direct optical imaging of the DLA hosts is difficult due to their proximity to the bright background quasars, especially in the case of faint DLA host galaxies. To improve the chance of detection, one can use the damped profile itself as a natural coronagraph (Smith et al. 1989; Møller & Warren 1993), or image below the Lyman Limit of a line of sight neighbour absorber (Steidel & Hamilton 1992; Christensen et al. 2009; Fumagalli et al. 2015).

Over the last decade, some progress has been made in understanding the nature of DLA galaxies via the use of correlations, especially in absorption properties. For example, DLAs appear to follow luminosity-metallicity (Møller et al. 2004), mass-metallicity (Ledoux et al. 2006; Prochaska et al. 2008) and spin temperature-metallicity (Kanekar et al. 2009, 2014) relations. The use of these correlations has helped optimize target selection for imaging studies: specifically, focused observations of high-metallicity DLAs have resulted in a significant increase in the number of identifications of $z \geq 2$ DLA hosts in recent years (e.g. Fynbo et al. 2010, 2011, 2013; Péroux et al. 2011, 2012; Noterdaeme et al. 2012a; Bouché et al. 2012; Krogager et al. 2013; Jorgenson & Wolfe 2014; Hartoog et al. 2015; Zafar et al. 2017). This has allowed a global description of metallicity scaling relations in DLA host galaxies, and their evolution with redshift (Møller et al. 2013; Neeleman et al. 2013), especially the mass-metallicity relation in DLAs, whose predictions have recently been verified by independent methods (Christensen et al. 2014). However, it should be recalled that a pre-requisite for an imaging study is that the DLA host be bright enough to be imaged; this effectively limits continuum studies of DLA hosts, similar to the case of a flux-limited sample. Specifically, while the HI selection allows to select a sample including low luminosity galaxies, the majority of DLA hosts are still undetectable in optical or near-infrared (IR) imaging studies due to the steep dependence of luminosity on metallicity (Møller et al. 2004; Fynbo et al. 2008).

The pre-selection of the highest metallicity systems for emission searches in many current observing programmes is thus in reality a flux-limiting sample pre-selection. While this has significantly increased the efficiency of those programmes (to a success rate of $\approx 50\%$ (Krogager et al. 2017)), one is restricted to studies of only a small fraction of the population. Imaging studies that do not have such pre-selection have a far lower success rate in imaging the DLA hosts (Charlot & Fall 1991; Lowenthal et al. 1995; Le Brun et al. 1997; Lanzetta et al. 1997; Guillemin & Bergeron 1997; Turnshek et al. 2001; Warren et al. 2001; Møller et al. 2002; Colbert & Malkan 2002; Kanekar et al. 2002; Lacy et al. 2003; Chen & Lanzetta 2003; Rao et al. 2003; Kulkarni et al. 2006; Chun et al. 2006; Straka et al. 2010; Battisti et al. 2012; Fumagalli et al. 2014, 2015; Srianand et al. 2016).

Because high metallicity traces more massive, and therefore larger, galaxies a side effect of metallicity pre-selection is that the median impact parameter of the detected hosts is larger for those samples. This effect was predicted by Møller et al. (2004); Fynbo et al. (2008) and has been verified observationally by Krogager et al. (2012). Therefore, both long-slit and integral-field-unit observations of high-metallicity DLA hosts may miss the target completely if the field of view is small. For example,

Wang et al. (2015) reported H α non-detections of 3 hosts out to impact parameters of only ≈ 12.5 kpc and used this to place limits on their star formation rates (SFRs). However, Krogager et al. (2017) investigated this question for several complete samples containing a large variety of DLA observations, and found that the fraction of non-detections precisely matches that predicted based on metallicity and limited field coverage. Latest, Neeleman et al. (2017) reported [CII] 158 μm emission at impact parameters 45 and 18 kpc from two DLAs at $z \approx 4$, confirming that even at this redshift the impact parameter will affect detection probability.

Thus, while much work remains to be done in characterizing the stellar properties of DLA hosts, it is clear that significant progress has been made in this field over the last decade. The situation is much worse in studies of the neutral gas that fuels this star formation, despite the fact that the neutral gas mass of DLA host galaxies and the gas distribution therein are critical pieces in understanding galaxy evolution. Unfortunately, the weakness of the HI 21cm line has meant that only a handful of DLAs and sub-DLAs have so far been searched for HI 21cm emission, and all at low redshifts, $z \lesssim 0.1$ (Kanekar et al. 2001; Bowen et al. 2001; Kanekar & Chengalur 2005; Briggs & Barnes 2006; Mazumdar et al. 2014; Chengalur et al. 2015). So far, only one DLA and one sub-DLA have been detected and mapped in HI 21cm emission (Bowen et al. 2001; Chengalur & Kanekar 2002; Briggs & Barnes 2006; Chengalur et al. 2015), at $z \approx 0.006 - 0.009$, with fairly tight limits ($\approx \text{few} \times 10^9 M_{\odot}$) available on the HI mass of three other systems (Mazumdar et al. 2014). Despite this difficulty in measuring the atomic gas content of individual DLA systems, the connection between DLAs and HI emission in low redshift galaxies has been made statistically by Zwaan et al. (2005). They show that the characteristics of low- z DLAs are consistent with their originating in gas discs of galaxies like those in the $z = 0$ population.

Similarly, until recently, the low sensitivity of mm-wave telescopes has meant that only a handful of searches have been carried out for molecular gas in emission in DLAs, yielding weak limits on the CO line luminosity, and thence on the molecular gas mass (e.g. Wiklind & Combes 1994). The lack of HI 21cm and CO emission detections in DLAs has also meant that we have little information on the transverse size of the absorbers. The neutral HI column density can typically only be measured along the sightline to the QSO, except in the rare cases when a single gravitationally-lensed or double background QSO can be used to constrain the spatial extent of the neutral gas (e.g. Ellison et al. 2007; Monier et al. 2009; Cooke et al. 2010; Zafar et al. 2011). Mapping of the HI 21cm absorption against the extended radio continuum (and thus measuring the spatial extent of the neutral gas), has also so far only been possible in a single DLA, at $z = 0.437$ towards 3C196 (Briggs et al. 2001; Kanekar & Briggs 2004).

With the advent of the Atacama Large Millimeter Array (ALMA), it is now finally possible to directly address the question of the molecular gas content of DLA host galaxies. We have hence initiated an ALMA survey for CO emission in a sample of DLA hosts, to measure their molecular gas masses, kinematical properties of the gas, determine the mass fractions in gas and stars, and their distributions, the star formation efficiencies, and to test whether DLA galaxies have similar properties as emission-selected galaxies at similar redshifts.

For our initial pilot ALMA survey, we chose to observe a sample of high-metallicity DLAs and sub-DLAs, at $z \approx 0.1 - 0.7$. This survey has already yielded the first detection of CO emission in a sub-DLA at $z = 0.101$ towards PKS 0439–433 (Neeleman et al.

Table 1. Observing log

ALMA ¹					
Date	freq. (GHz)	bandwidth (GHz)	channels (#)	resolution (MHz)	feature
27.12.14	132.61	2	128	15.625	Contin.
	134.38	1.875	3840	0.488	CO(2-1)
	144.61	2	128	15.625	Contin.
	146.61	2	128	15.625	Contin.
FORS2					
Date	exp time	seeing	GRISM	slit	$\lambda/\Delta\lambda$
17.04.15	2200 s	1''.2	600RI	1''.3	900
18.04.15	2200 s	0''.9	600RI	1''.3	900

[1] The ALMA observations were done with 40 antennas and a maximum baseline of 348.5 m. On-source time was ≈ 40 minutes, and the PWV was 5.5 mm.

2016b), originally selected as being part of a QSO-galaxy pair (Petitjean et al. 1996). In this paper, we describe our ALMA observations of a second DLA, at $z_{\text{abs}} = 0.7163$ towards J1323–0021 (SDSS J132323.78-002155.2). The absorber was originally detected by Rao et al. (2006) via Hubble Space Telescope (HST) spectroscopy. A companion galaxy was subsequently reported as a candidate DLA host by Hewett & Wild (2007), based on near-IR imaging data, but attempts to confirm the identification via detection of optical/NIR emission lines were so far unsuccessful.

Our ALMA data allow us to definitively identify the DLA host galaxy via the detection of CO(2-1) line emission, and to characterise its molecular gas content and distribution. We also present a new Very Large Telescope (VLT) Focal Reducer and low dispersion Spectrograph (FORS2) spectrum which confirms the identification, as well as new optimized reductions of archival VLT Spectrograph for INtegral Field Observations in the Near Infrared (SINFONI) and Ultraviolet Echelle Spectrograph (UVES) data. In addition re-calibrated Herschel and HST/STIS data are reduced and analyzed. The paper is organised as follows: Section 2 describes our new observations and data analysis, as well as our new reductions of archival data, Section 3 presents our results and the extracted physical parameters of the $z = 0.7163$ DLA host galaxy, while Sections 4 and 5 discuss the new results and summarize our conclusions. Throughout this paper, we assume a flat Λ cold dark matter (Λ CDM) cosmology with $H_0 = 70.4 \text{ km s}^{-1} \text{ Mpc}^{-1}$ and $\Omega_\Lambda = 0.727$ (Komatsu & et al. 2011).

2 OBSERVATIONS AND ARCHIVAL DATA

2.1 ALMA observations

The field of the $z = 0.7163$ DLA towards J1323–0021 was observed with ALMA using the band 4 receivers as part of project 2013.1.01178.S, on 27 December 2014 (log provided in Table 1). Observing conditions were below average for high-frequency studies, with an average precipitable water vapour measurement of 5.5 mm. The ALMA correlator was configured to use four spectral windows in dual polarization mode. A single high-resolution 1.875 GHz band, sub-divided into 480 channels, was centred at the redshifted CO(2-1) line frequency (134.3 GHz); this yielded a velocity resolution of $\approx 16.4 \text{ km s}^{-1}$ (after online Hanning-smoothing), and a total velocity coverage of 4185 km s^{-1} around

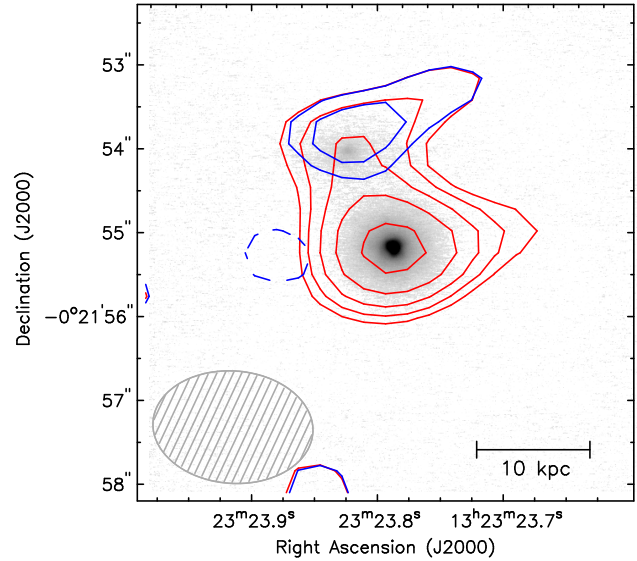


Figure 1. ALMA 140 GHz continuum image (red contours) overlaid on the AO K -band image from Chun et al. (2010) (kindly provided by Mark R. Chun); the ALMA beam ($1.91'' \times 1.35''$) is shown in the lower left corner. Note the extension of emission to the north of the QSO which matches the position of the galaxy detected in the infrared image. The contours start at 2σ and increase by factors of $\sqrt{2}$; the dashed contour is at -2σ . The blue contours are at the same levels, but are for a continuum image where a point source model at the quasar position has been subtracted from the U-V visibilities before imaging. The 140 GHz continuum emission from the galaxy is detected at 3.2σ significance.

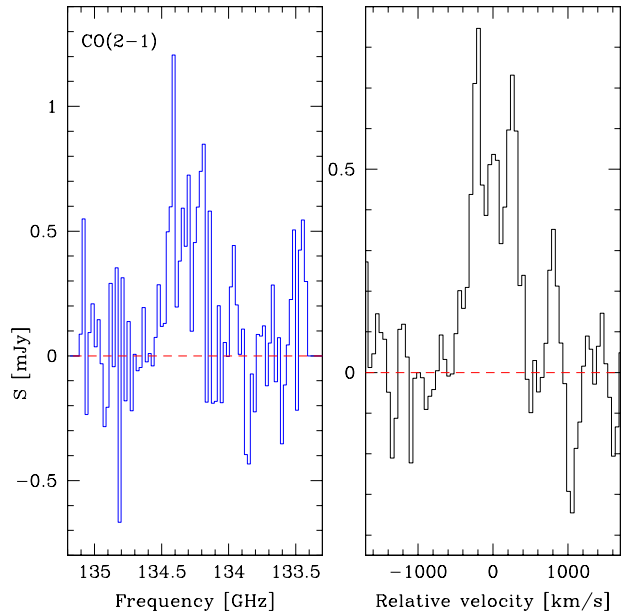


Figure 2. The CO(2-1) emission line spectrum: **Left panel:** The spectrum at the original velocity resolution of the spectral cube, 50 km s^{-1} , with flux density (mJy) plotted against barycentric frequency (GHz). **Right panel:** The spectrum slightly smoothed (to a resolution FWHM of $\approx 60 \text{ km s}^{-1}$) and here plotted against velocity, in km s^{-1} , relative to a redshift of $z = 0.7163$.

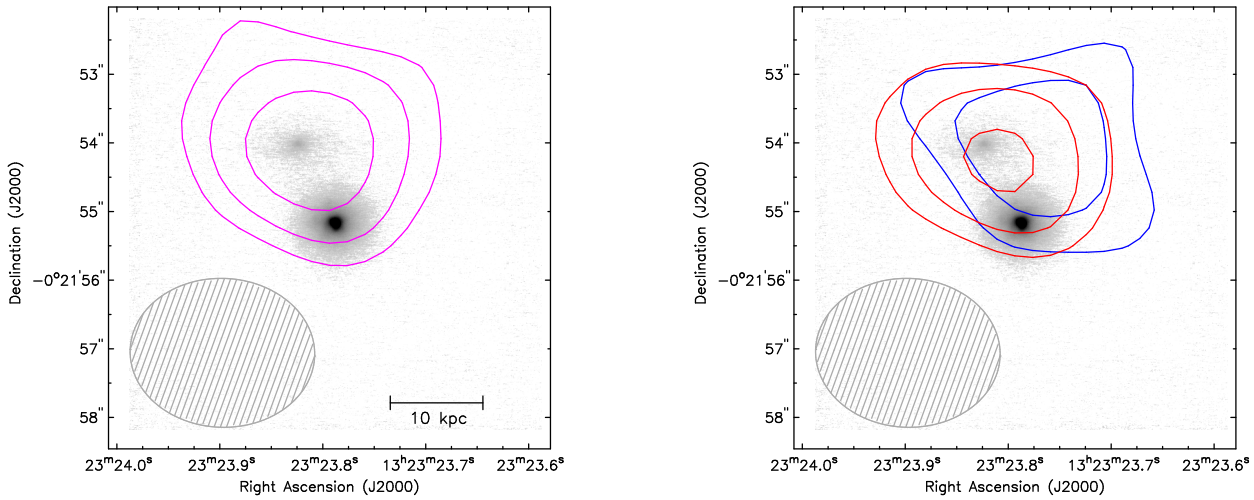


Figure 3. [A] **Left panel:** The total intensity CO(2-1) emission image (in purple contours) overlaid on the near-IR K -band image of Fig. 1. The contours start at 3σ significance and increase by factors of $\sqrt{2}$. The synthesized beam is shown in the lower left corner, and is of size $2.7'' \times 2.2''$. [B] **Right panel:** Total intensity CO images of the low (-400 km s^{-1} to -200 km s^{-1}) and high (-200 km s^{-1} to $+400 \text{ km s}^{-1}$) velocity parts of the CO(2-1) emission line, in blue and red, respectively, overlaid on the near-IR K -band image. The contour levels are the same as in the left panel. It is clear that the high-velocity CO emission is spatially aligned with the rest-frame optical emission of the DLA host, while the low-velocity CO emission is slightly offset from the optical emission. Note that the fact that both maps appear to cover the sightline towards the QSO (the bright source in the centre of the near-IR image) is likely an artefact of the synthesized beam.

the DLA redshift. To obtain continuum data the three other bands were used in low-resolution mode, giving 2 GHz bandwidth and 128 channels each. Forty 12-metre ALMA antennas were used for the observations, with a maximum baseline of 348.5 m. A standard observing strategy was used, with a phase calibrator (J1319–0049) observed every ≈ 8 min, and a bandpass calibrator (J1256–0547) observed for 15 min. Flux calibration was obtained through observing the quasar 3C279, whose absolute flux scale is frequently verified by the ALMA observatory. The total on-source time was approximately 40 minutes.

The data editing, calibration and imaging was carried out in the CASA (Common Astronomy Software Applications) package, using standard procedures. Stable phase solutions were found for most antennas, except for a period of ≈ 10 minutes in the middle of the observing run. Data for approximately half the antennas were disregarded for that period. A continuum image of the field was made by combining data from all four observing bands, excluding the channels containing line emission. This image was made using “robust” weighting, with a Briggs parameter of 0.5, and has a root-mean-square (RMS) noise level of $16.4 \mu\text{Jy/beam}$. We clearly detect continuum emission from the quasar, with a flux density of 0.14 mJy . This is, however, too faint for the purpose of self-calibration. The continuum map shows a tantalising extension to the North (see Fig. 1), exactly in the direction of the candidate galaxy reported $1''.1$ to the NE of the QSO (Hewett & Wild 2007), and at $1''.25$ to the NE in a higher resolution adaptive-optics image (Chun et al. 2010). To investigate this further, we re-imaged the field after subtracting out a point source model at the quasar position from the U-V visibilities. Both the unsubtracted (red contours) and the point-source-subtracted (blue contours) data are shown in Fig. 1. The 140 GHz continuum flux density at the position of the DLA host galaxy is $53 \mu\text{Jy}$, which corresponds to a 3.2σ detection. The position of the centroid of the continuum emission is in excellent agreement with the galaxy position in the optical image.

A data cube covering the CO(2-1) line redshifted to the red-

shift of the DLA was made by imaging the high-resolution visibility dataset in 50 km s^{-1} -wide spectral channels. Since the data were obtained with slightly higher spatial resolution than requested, we tapered the visibilities beyond $75 \text{ k}\lambda$ during the imaging, in order to improve the surface brightness sensitivity. The resulting spectral cube has a synthesized beam of extent $2.7'' \times 2.2''$ and an RMS noise of 0.25 mJy/beam per 50 km s^{-1} channel. The above angular resolution translates to a spatial resolution of $\approx 19.8 \text{ kpc} \times 16.1 \text{ kpc}$ at the DLA redshift, $z = 0.7163$. This relatively coarse spatial resolution excludes the possibility that we may be resolving out some of the CO emission.

CO(2-1) emission is clearly detected in the cube, with a peak line flux density of $(1.70 \pm 0.25) \text{ mJy}$ (i.e. at $\approx 7\sigma$ significance). The CO(2-1) line profile is shown in Fig. 2; this was obtained by summing all emission over an aperture of $1.5''$ centred on the optical galaxy. The profile is seen to display the steep sides and relatively flat central part referred to as “boxy” profiles or double-horned (Davis et al. 2011), although the signal-to-noise ratio (S/N) is relatively low. We obtained a total CO intensity image by adding the flux from all channels over the central range of $\approx 500 \text{ km s}^{-1}$, without applying any spatial masking to the channel maps. Fig. 3[A] shows an overlay of this total CO intensity image on the near-IR image; it is clear that the CO emission is centred on the near-IR emission from the galaxy and not on the QSO. With the clear detection of the CO(2-1) emission line, we identify the neighbouring galaxy as the DLA host: this constitutes the first confirmation of the identification of a DLA host galaxy via molecular line emission. The velocity-integrated CO(2-1) line flux density is $S_{\text{int}} = (0.50 \pm 0.05) \text{ Jy km s}^{-1}$; the measured flux densities are listed in Table 4.

In addition to the integrated CO image, we also produced two maps where we separately summed the fluxes from the low velocity CO peak (over the velocity range -400 km s^{-1} to -200 km s^{-1}) and the high velocity peak ($+200 \text{ km s}^{-1}$ to $+400 \text{ km s}^{-1}$). Those are both plotted in Fig. 3[B], as blue and red contours respectively.

MAP	Flux (mJy)
250 μm	11.4 \pm 1.0
350 μm	8.5 \pm 1.1

Table 2. Herschel/SPIRE photometry of the DLA galaxy, corrected for the fraction of the flux from the QSO (assumed from ALMA data, see text). The cited errors include only the photometric errors, not possible systematic errors from the QSO fraction correction.

It is seen that the red set of contours fit the position of the galaxy well, while the centroid of the blue contours is offset by $0''.9$ (6.6 kpc) to the West indicating that the molecular gas has a spatially resolved kinematic structure. We shall return to this in more detail in Sect. 3.2.

2.2 Herschel data

The QSO was observed with Herschel/SPIRE (Griffin et al. 2010) on July 31, 2011 in the 250, 350 and 500 μm bands (OBSID: 1342224987, PI: V. Kulkarni). We obtained the re-calibrated maps from the Herschel science archive.

The effective FWHM in the three bands are 17.6, 23.9, and 35.2 arcsec, respectively, and because of the small separation between the QSO and DLA galaxy, it was not possible to deconvolve their emission into two distinct components. Visual inspection of the maps showed that the QSO plus DLA galaxy is clearly detected in the 250 and 350 μm maps, but not in the 500 μm map, which was excluded from further analysis.

To measure the integrated flux, the Herschel level 2 maps were divided by the effective beam area and multiplied by the pixel sizes to get maps in units of Jy/pixel. We performed aperture photometry following the description of SPIRE point source photometry in Pearson et al. (2014) choosing a small aperture size, and including an aperture correction to derive the total flux. Errors were obtained using the same apertures on the Herschel error maps and adding errors in quadrature. The integrated aperture flux was verified using the data analysis software 'Herschel Interactive Processing Environment (HIPE)' (Ott 2010).

The fractional flux detected in the ALMA continuum band from the DLA galaxy relative to the QSO is 0.27 ± 0.07 . To estimate the Herschel flux from the DLA galaxy alone we assumed that the fractional flux detected in the ALMA continuum band from the DLA galaxy is the same also at shorter wavelengths. The final results are reported in Table 2. We discuss, and validate, this assumption in Sect. 3.4.3.

2.3 VLT-FORS2 data

The galaxy identified in the ALMA image as the absorber, was also part of a VLT-FORS2 programme to obtain spectra of DLA galaxy candidates (programme ID 095.A-0890(A); PI: L. Christensen). The galaxy was observed on 17 and 18 April 2015, with FORS2 long-slit spectroscopy using the grism 600RI, which covers the wavelength range 5120 – 8250 \AA at a spectral resolution of $R \sim 900$ with the chosen slit width of $1.3''$. The total integration time was 4×1100 seconds on target with the slit aligned at PA = 42° East of North, to cover both the QSO and the candidate galaxy based on the relative coordinates in Rao et al. (2011). The observing conditions were non-photometric, and the seeing mea-

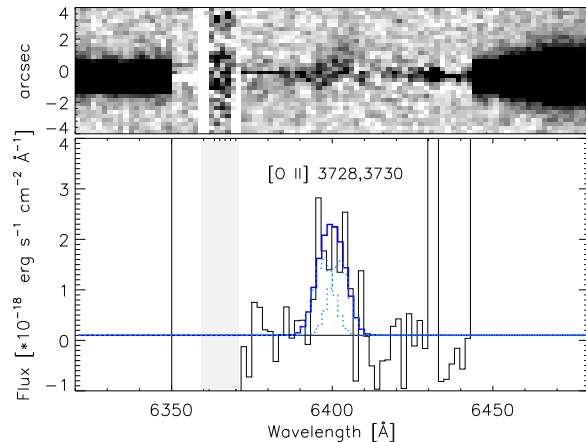


Figure 4. **Upper panel:** two-dimensional VLT-FORS2 spectrum around the [OII] emission line from the $z = 0.7163$ DLA host galaxy. The QSO emission has been subtracted in the range 6350 – 6440 \AA ; some residuals from this subtraction can be seen in the inner few rows. Excess emission is seen at the expected wavelength and impact parameter. **Lower panel:** 1D spectrum extracted in the aperture from $0.25'' - 2.5''$ above the QSO trace; The fit of the [OII] doublet is overlaid on this spectrum, the two individual components as dotted blue lines, the sum as a full blue line.

asured in the spectra varied in time and wavelength over the range $0.9 - 1.2''$, with better values measured on April 18 (Table 1).

The VLT-FORS2 data were analysed in the standard manner with bias subtraction, flat fielding, and wavelength calibration, and sky background subtraction using a median value from pixels adjacent to the QSO and the galaxy. To flux calibrate the data, we used an observation of the spectrophotometric standard star EG274 observed on 17 April. However, as the night was not photometric systematic flux calibration errors are expected, along with slit losses. Comparing the flux-calibrated QSO spectrum with a spectrum obtained in the Sloan Digital Sky Survey (SDSS) on 19 February 2001, we find that the FORS2 spectrum has a 40% lower flux level than the SDSS spectrum over the entire wavelength range. A further comparison of the FORS2 R -band acquisition image with an SDSS r -band image reveals that ten bright stars in the field have the same magnitudes (within 0.01 mag.) in the FORS2 and SDSS images, while the QSO in the FORS2 image is 0.1 mag fainter than in the SDSS image. We cannot determine how much the variation of the flux level in the FORS2 spectra is due to intrinsic time variations of the QSO flux or slit losses and hence simply report the measured flux from the DLA host galaxy, with the caveat that the flux is likely to be low by a factor of ≈ 2 .

A high-resolution Keck K -band image, obtained with the use of adaptive optics, shows a spatial offset of $1''.25$ between the galaxy and the QSO (Chun et al. 2010). This implies that the two objects are blended in the moderate seeing of our FORS2 observations. A careful subtraction of the QSO emission is therefore necessary to recover any spectral signatures from the galaxy. To search for the [OII] $\lambda\lambda 3727, 3729$ doublet, we assume that the QSO continuum emission is a pure power law in two wavelength ranges immediately bluewards and redwards of the expected [OII] emission feature, and that the spatial point spread function (PSF) modelled in the adjacent wavelengths does not depend on wavelength. The measured QSO flux is then scaled to the different spectral wavelengths and subtracted out, a process known as spectral PSF (or SPSF) subtraction. The same approach has been used to find metal

emission lines from high-redshift DLA galaxies (Weatherley et al. 2005; Fynbo et al. 2013; Krogager et al. 2013). Fig. 4 shows the result of the subtraction, which reveals a clear detection of excess emission at exactly the spatial position of the galaxy.

The [OII] line doublet is not well resolved at the relatively low FORS2 resolution and we therefore perform a simultaneous fit to both lines, where we lock the full width at half maximum (FWHM) of the two lines to be identical, but allow the flux ratio of the lines to vary freely. We find that the FWHM is $<300 \text{ km s}^{-1}$ with a heliocentric wavelength corresponding to [OII] at $z = 0.7165 \pm 0.0004$, where the redshift uncertainty reflects the uncertainty of wavelength position in the emission line fit from propagated statistical errors. There are additional systematic errors from strong subtraction residuals close to the quasar trace which we take into account as follows. The SPSF subtraction at the expected galaxy position (from imaging) is excellent with insignificant residuals, and the extracted [OII] line at this position provides a redshift $z = 0.7176 \pm 0.0004$. We take the difference here to be the result of the sum of systematic and statistical errors, plus possibly a component from rotation (as suggested from Fig. 4). Conservatively we assign it all to the combined error and adopt the average ($z = 0.7170 \pm 0.0006$) as the best redshift estimator where the error spans both extremes.

The integrated flux from the two components is $(2.8 \pm 0.3) \times 10^{-17} \text{ erg cm}^{-2} \text{ s}^{-1}$, after correcting for Galactic extinction of $E_{B-V} = 0.024$ (Schlafly & Finkbeiner 2011), but not for intrinsic extinction in the DLA galaxy itself. The full results of the FORS2 analysis are listed in Table 4. We note, in passing, that the low [OII] emission line flux is consistent with the non-detection of [OII] emission by Straka et al. (2015).

2.4 VLT SINFONI data

Péroux et al. (2011) presented VLT SINFONI *J*-band integral field unit spectroscopy of the field of the $z = 0.7163$ DLA. They reported a non-detection of $\text{H}\alpha$ emission from the candidate host galaxy. To complete our multi-wavelength study, we retrieved the SINFONI dataset (programme ID: 079.A-0673) from the European Southern Observatory (ESO) archive and re-reduced it. The SINFONI *J*-band spectra cover the spectral range 11000 – 14000 Å at a resolution of $R \sim 2000$, and the field of view 8 arcsec \times 8 arcsec. A total of 13×900 seconds of integration was split over three different observing nights in 2007, using a dither pattern for sky subtraction. A large offset dither pattern avoids nodding into the galaxy, thus avoiding over-subtraction.

Our data processing was done with the recent version (2.6) of the SINFONI pipeline; the individual steps involved the same basic routines used by Péroux et al. (2011), apart from the flux calibration and correction of telluric absorption lines. Specifically, telluric absorption line corrections may cause differences in our results compared to the previous reported ones. We do not initially include a telluric correction of the data cubes using the calibration observation of a hot star just before or after the science exposures as implemented in the pipelines, but instead we derive the correction directly from the QSO spectrum. We find that this is particularly important in the spectral region between the *Y* and *J* bands, where the $\text{H}\alpha$ emission line from the DLA galaxy falls. Observations on each of the three observing nights of hot B-type stars with known magnitudes from the Hipparcos catalogue and known spectral types were used for flux calibration.

To extract information on the galaxy, we first construct an intermediate-band filter image by summing over an $\approx 50 \text{ nm}$ wide

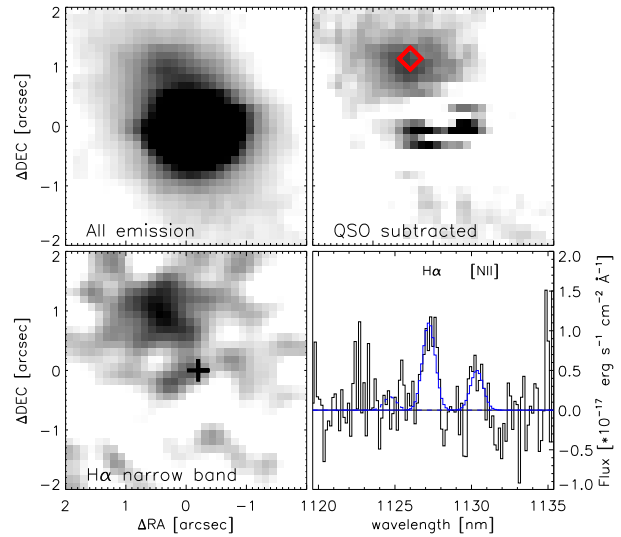


Figure 5. Images constructed from the VLT SINFONI data cube as described in the text. **Upper left:** Continuum image with a width of $\approx 50 \text{ nm}$ centred at 13500 nm, **Upper right:** Same wavelength region after PSF subtraction. The red diamond marks the centroid of the object seen in the AO *K*-band image (Fig. 1 and Chun et al. (2010)), **Lower left panel:** A narrow-band (10 Å) image centred on the redshifted $\text{H}\alpha$ line at $z = 0.7171$, after subtracting out the continuum emission; the location of the QSO is marked by a '+' sign. **Lower right panel:** The $\text{H}\alpha$ + $[\text{NII}]$ emission line spectrum extracted by selecting spaxels with significant $\text{H}\alpha$ emission in the image of the bottom left panel, from which the galaxy continuum emission has been subtracted out.

region in the data cube centred on 13500 Å. The upper left hand panel in Fig. 5 shows the resulting image, which is clearly dominated by the QSO emission, but also shows an extension of fainter emission to the North-East at a distance of $1''.2$ (equal to the impact parameter of the candidate DLA host). Fitting a 2-dimensional Moffat function to the QSO location gives a spatial FWHM of $0.9'' \times 0.7''$ in the East-West and North-South directions, respectively. We then model the QSO emission by fitting a 2-dimensional Moffat profile with a spatial location and an FWHM that vary smoothly with wavelength through the data cube and subtract this model from the initial data cube. After this, the same spectral region of the data cube is summed as illustrated in the upper right panel in Fig. 5. Some residuals within the FWHM of the QSO position are seen, but the continuum emission of the DLA galaxy is now clearly visible in the image.

We extract a one-dimensional spectrum of the galaxy within an elliptical aperture of $2'' \times 1.5''$ by coadding spatial pixels (“spaxels”) associated with the galaxy. After application of corrections for telluric absorption and flux calibration, the continuum flux level in the chosen region around $\lambda = 13500 \text{ Å}$ is measured to be $(6.7 \pm 1.3) \times 10^{-18} \text{ erg cm}^{-2} \text{ s}^{-1} \text{ Å}^{-1}$. This flux density corresponds to an AB magnitude of 19.9 ± 0.25 at this wavelength. The large uncertainty reflects the added uncertainty from the QSO subtraction residuals. At the bluest end of the spectral range, the 1-dimensional spectrum corresponds to a magnitude $m_{11200} = 20.20 \pm 0.20$. We include those continuum magnitudes in our analysis of the spectral energy distribution of the galaxy in Sect. 3.4.1.

The extracted spectrum of the galaxy also shows a clear $\text{H}\alpha$ emission line at $\lambda = 11272.2 \pm 0.8 \text{ Å}$. We create a pure narrow-band $\text{H}\alpha$ image by co-adding the relevant wavelength slices around

the emission line and subtracting the adjacent continuum emission from the galaxy; the result is shown in the lower left panel of Fig. 5. To extract the final, telluric absorption corrected, emission line spectrum we first define a $2'' \times 1.5''$ rectangular aperture centred on the DLA galaxy. We sum all spaxels of the original data cube within this aperture, apply the telluric correction determined from spaxels only containing QSO continuum, and finally subtract the continuum from the resulting 1D spectrum. The spectrum is shown in the lower right hand panel of Fig. 5 where we also see a clear detection of [NII] $\lambda 6584$ emission. The other line of the doublet [NII] $\lambda 6548$ is not detected, but this is consistent with the noise-level of the data. The emission lines indicate a galaxy redshift of $z = 0.7171 \pm 0.0001$.

Fitting Gaussian functions to the emission lines, we measure a line flux of $f(\text{H}\alpha) = (12.0 \pm 3.9) \times 10^{-17} \text{ erg cm}^{-2} \text{ s}^{-1}$ and $f(\text{[NII]}) = (5.6 \pm 1.8) \times 10^{-17} \text{ erg cm}^{-2} \text{ s}^{-1}$. The $\text{H}\alpha$ line is resolved and has an FWHM of $238 \pm 34 \text{ km s}^{-1}$, after correcting for the instrumental resolution. On both the extracted J-band (m_{13500}) and narrow-band images we measure the position of the DLA galaxy relative to the QSO. The resulting values (PA and impact parameter) are provided in Table 4.

In passing we note that we also detect an emission-line system at $z = 1.38$, at an impact parameter to the QSO sightline of $2.3''$ to the North-East. This system was serendipitously discovered by Péroux et al. (2011), and does not have a corresponding detection in continuum emission (Hewett & Wild 2007; Rao et al. 2011; Chun et al. 2010). Additionally, given the high line flux ratio $\log f(\text{[OIII]})/f(\text{H}\beta) \sim 1$ which indicates a hard ionising source, this system is most likely an extended emission line region at the redshift of the quasar, and ionized by it. This emission-line system does not in any way contaminate the results obtained for the DLA host galaxy.

2.5 VLT UVES and HST STIS data

We obtained the advanced data product VLT-UVES spectrum of the QSO, presented in Péroux et al. (2006), from the ESO data archive. We corrected wavelengths to the heliocentric frame and converted from air to vacuum wavelengths before combining individual exposures to produce the final spectrum. The saturated absorption lines in the spectrum, such as FeII $\lambda 2344$, $\lambda 2382$, and $\lambda 2600$, show multiple spectral components at redshifts in the range $z = 0.71531 - 0.71668$, equivalent to a total velocity spread of $\approx 240 \text{ km s}^{-1}$. Using the definition of Δv_{90} (Prochaska & Wolfe 1997), which is based on the optical depth profile of an unsaturated low ionization line, we measure a velocity spread of $\Delta v_{90} = 141 \text{ km s}^{-1}$ from the MnII $\lambda 2576$ absorption line (see Table 4).

The large velocity spread and number of spectral components makes it difficult to assign a unique redshift to the absorption system. Also here we then use the definition of Δv_{90} and assign the median optical depth ($z_{\tau:50}$, the redshift at which 50% of the optical depth is on either side) as the effective redshift of the system. Using this definition we find $z_{\tau:50} = 0.71612$ which implies that the absorber is kinematically offset from the $\text{H}\alpha$ emission by $171 \pm 18 \text{ km s}^{-1}$. In addition we determine the redshift at which the system has its largest optical depth, $z_{\tau:\text{max}} = 0.71625$.

Péroux et al. (2006) report that 16 individual components make up the complex line profile of the DLA and derive a metallicity $[\text{Zn}/\text{H}] = 0.61 \pm 0.20$, for $\log[N(\text{HI})/\text{cm}^{-2}] = 20.21^{+0.21}_{-0.18}$ (obtained by Khare et al. 2004). We note that the identification of the absorber as a DLA or a sub-DLA and the value of the metallicity is critically dependent on the HI column density estimate.

Specifically, Rao et al. (2006) derive $\log N(\text{HI}) = 20.54^{+0.16}_{-0.15}$ from the same HST Space Telescope Imaging Spectrograph (STIS) spectrum. We therefore downloaded the STIS data from the HST archive and performed an independent determination of the HI column density. Our result agrees with the later analysis of Rao et al. (2006), but does not rule out the original result of Khare et al. (2004). In the following analysis, we will use our estimate, $\log[N(\text{HI})/\text{cm}^{-2}] = 20.4^{+0.3}_{-0.4}$, where the adopted errors span the full 1σ range of the two other estimates. This then implies a gas-phase metallicity of $[\text{Zn}/\text{H}] = +0.4 \pm 0.3$. We note that Neeleman et al. (2016a) did not include this spectrum in their sample because its S/N is lower than their threshold of 4.

3 RESULTS

3.1 The molecular gas mass

The velocity-integrated CO J=2-1 line flux density is $S_{\text{int}} = (0.50 \pm 0.05) \text{ Jy km s}^{-1}$. This can be used to compute the molecular gas mass of the $z = 0.7163$ galaxy if we know the CO-to- H_2 conversion factor α_{CO} and the nature of the CO excitation. Both of these depend on the nature of the galaxy: for example, spiral disk galaxies like the Milky Way have $\alpha_{\text{CO}} \approx 4 M_{\odot} (\text{K km s}^{-1} \text{ pc}^2)^{-1}$, while QSOs and starburst galaxies (e.g. ultraluminous infrared galaxies and sub-millimetre galaxies) have far lower values, $\alpha_{\text{CO}} \approx 1 M_{\odot} (\text{K km s}^{-1} \text{ pc}^2)^{-1}$, both after including a factor of 1.36 to correct for the contribution of helium (e.g. Bolatto et al. 2013; Carilli & Walter 2013). The conversion factor also has a strong dependence on metallicity, with far higher α_{CO} values ($\gtrsim 30 M_{\odot} (\text{K km s}^{-1} \text{ pc}^2)^{-1}$) obtained in low-metallicity systems (e.g. Leroy et al. 2011) than in high-metallicity galaxies ($\alpha_{\text{CO}} \lesssim 4 M_{\odot} (\text{K km s}^{-1} \text{ pc}^2)^{-1}$). In the present case, the high metallicity of the DLA host galaxy indicates a low α_{CO} value.

Next, CO in QSOs and starburst galaxies has typically been found to be thermalized up to the J= 3 level, with sub-thermal excitation of the higher-J levels (e.g. Weiß et al. 2007; Danielson et al. 2011). Conversely, even the J= 2 level is typically sub-thermally excited in spiral galaxies (e.g. Fixsen et al. 1999; Dannerbauer et al. 2009; Carilli & Walter 2013). In thermal equilibrium, the brightness temperature of the CO J= 2 - 1 line would be equal to that of the J= 1 - 0 line, while in the Milky Way, the J= 2 - 1 brightness temperature is ≈ 0.6 times that of the J= 1 - 0 line. We will assume sub-thermal excitation of the J= 2 level and a brightness temperature line ratio of $r_{21} \approx 0.6$ ($r_{21} = L'_{\text{CO}(2-1)}/L'_{\text{CO}(1-0)} = S_{\text{CO}(2-1)}/(4 \times S_{\text{CO}(1-0)})$) for the J= 2 - 1 and J= 1 - 0 lines, consistent with the assumption of a Milky-Way value for α_{CO} .

For the assumed Λ CDM cosmology, the CO J= 2-1 flux density of $S_{\text{int}} = (0.50 \pm 0.05) \text{ Jy km s}^{-1}$ implies a CO J= 1 - 0 flux density of $(0.20 \pm 0.02) \text{ Jy km s}^{-1}$, and thence, a CO J= 1 - 0 line luminosity of $L'(1-0) = (5.55 \pm 0.55) \times 10^9 \text{ K km s}^{-1} \text{ pc}^2$. Using $\alpha_{\text{CO}} = 4.2 M_{\odot} (\text{K km s}^{-1} \text{ pc}^2)^{-1}$ (recommended by Bolatto et al. 2013) then yields a total molecular gas mass of $M_{\text{mol-gas}} = (2.33 \pm 0.23) \times [\alpha_{\text{CO}}/4.2] \times (0.6/r_{21}) \times 10^{10} M_{\odot}$ for the DLA host galaxy. Conversely, if we were to assume that the DLA host contains an obscured starburst, with $\alpha_{\text{CO}} \approx 1$ and $r_{21} \approx 1$ (i.e. that the J= 2 level is thermalized), we obtain a molecular gas mass of $M_{\text{mol-gas}} = (3.5 \pm 0.35) \times [\alpha_{\text{CO}}/1.0] \times (1.0/r_{21}) \times 10^9 M_{\odot}$. Since the SFRs estimated from both the $\text{H}\alpha$ line and the dust continuum are low ($\lesssim 5 M_{\odot} \text{ yr}^{-1}$ see Sections 3.4.2 and 3.4.3), we

consider the starburst scenario to be unlikely. This is further supported by the galaxy’s gas-to-dust ratio (see Sect. 4.4). We therefore conclude that the most likely scenario is the former, and that the molecular gas mass of the DLA host galaxy is likely to be very high. The values of α_{CO} applied here already include the correction (1.36) for He.

3.2 Kinematics of the molecular, neutral and ionized gas

In Fig. 6, we provide an enlarged view of the CO J= 2 – 1 emission line profile shown in the right panel of Fig. 2. The flat-topped appearance of a “boxy” profile (Davis et al. 2011) is here evident. The flat profile appears to consist of three individual CO velocity components, but the details of this sub-structure is difficult to verify at the current S/N and must await better data. Overlaid in Fig. 6 we show the spectral components of the ionized gas seen in the VLT-SINFONI and VLT-FORS2 emission spectra (marked in red), and the absorbing DLA gas seen in the VLT-UVES spectrum (blue). For the absorption profiles, we mark the velocity spread containing 90% of the integrated optical depth of low-ionization unsaturated metal lines, Δv_{90} .

Curiously, Fig. 6 indicates that the H α emission is kinematically related only to the two highest redshift molecular components, while the lowest-redshift molecular feature appears to be kinematically distinct from both the optical emission and absorption lines. The lowest-velocity molecular peak spans the bins from which we produced the blue contour map in Fig. 3, where it was seen that this peak also appears spatially offset from the optical galaxy. The velocity span of the metal-line absorption lies kinematically between the reddest and bluest CO velocity components, which are plotted as red and blue contours in Fig. 3.

3.2.1 Centroid positions of emission sub-components

In order to address this issue of position of the various emission sub-components quantitatively, we determine the positions of the dust and of the red and blue CO components. For DLA hosts, this information is traditionally provided in the form of the position angle (PA) and the impact parameter (b_{DLA}), relative to the quasar. Based on the high resolution K -band data, Chun et al. (2010) reported $(\text{PA}, b_{\text{DLA}}) = (24.5^\circ, 1''.25)$. From the images of the dust continuum, the red CO component, and the blue CO component, we obtain $(\text{PA}, b_{\text{DLA}}) = (17 \pm 8^\circ, 1''.46 \pm 0''.2)$, $(32 \pm 14^\circ, 1''.03 \pm 0''.3)$, and $(-18 \pm 14^\circ, 1''.15 \pm 0''.3)$, respectively. It is apparent that the first two sets of values agree well with the optical position of Chun et al. (2010), whereas the last does not. More specifically, measuring the distance between the K -band position of the host and the centroid of the image of the blue CO component, we find $0''.9 \pm 0''.3$. This is statistically significant evidence that the blue CO component is spatially offset from the other three (optical, dust, red CO) components.

From the results summary in Table 4 we see that there is agreement (to within the errors) between the relative position of the DLA galaxy detected in K -band, J -band, dust continuum, H α and “red CO component”, i.e. all of those emission components of the Damped absorber appear to be centred on the optical galaxy.

3.3 The CO line width and the dynamical mass

As noted in Sect. 2.1 the CO J=2-1 line profile matches the definition of a boxy profile. To obtain measures for the line width which

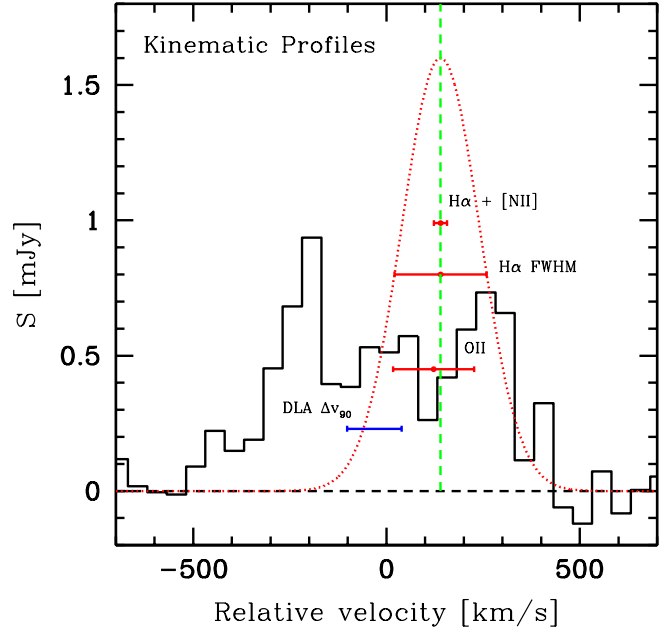


Figure 6. Detailed kinematical structure of the three gas components: molecular (black histogram), neutral (in absorption, blue horizontal bar), and ionized (red). All velocities are relative to $z = 0.7163$. The rest-frame optical emission lines are seen to be aligned with the central and the highest redshift peak of the molecular gas. Error bars on H α + [NII] and [OII] points are measurement errors while the bar marked “H α FWHM” spans the FWHM of the H α line. To assist the comparison we overplot the Gaussian fit to the H α line from Fig. 5.

are directly comparable to those of the COLD GASS galaxy sample (Saintonge et al. 2011) we use the same fitting formula for a double-horn profile (equation A2 in Tiley et al. 2016). A fit of this function to the unsmoothed data (shown in Fig. 7, left panel) finds a CO central redshift of $z = 0.71645(9)$, a W50 of $647 \pm 54 \text{ km s}^{-1}$ and W20 of $652 \pm 54 \text{ km s}^{-1}$ (uncorrected for inclination). Our CO map does not have the resolution to obtain an inclination angle of the disk, but from the high resolution AO image presented by Chun et al. (2010) (their figures 1 and 2) we estimate that the inclination is in the range $40\text{--}48^\circ$ (including also the effect of a slightly elongated residual PSF). Using the most conservative value we get $W50/\sin(48^\circ) = 871 \text{ km s}^{-1}$.

This is an extremely large velocity width for CO emission, comparable to those obtained in the most massive sub-millimetre galaxies and QSOs (e.g. Carilli & Walter 2013). As noted above, it is possible that the bluest feature of the profile may be due to a separate object which is kinematically detached from the main galaxy. In particular the H α line is offset from the CO central redshift. To test this possibility we also perform a second fit using the same functional form, but now locking the central frequency of the fit to that of the H α line. The fit is restricted to the spectral range from -200 km s^{-1} and above, and gives $W50 = 378 \pm 52 \text{ km s}^{-1}$, $W20 = 384 \pm 52 \text{ km s}^{-1}$ which is more in line with typical galaxies of similar stellar mass. In addition we fit a single gauss profile to the remaining blue peak which covers the spectral range used for the blue contours in Fig. 3. The best fit gauss has $\sigma = 61 \text{ km s}^{-1}$ and an offset of -212 km s^{-1} relative to the fiducial DLA redshift (0.7163), resulting in a total offset between this blue component and the H α line of 352 km s^{-1} . The combined fit is shown in the

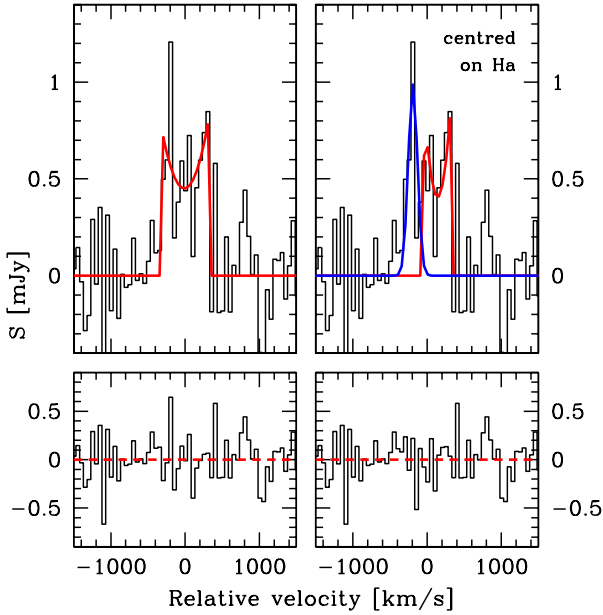


Figure 7. *upper panel, left:* Double-horn profile fit to the CO(2-1) line (red); *upper right:* fit using the same double-horn profile function but forced to be centred at the same redshift as the H α line (red), plus a single gauss profile fit to the remaining peak (blue). *Lower panels:* residuals.

right panel of Fig. 7. The flaring parameter ($R_{2.5} = W_{20}/W_{50}$) is found to be 1.01 and 1.02 for the two fits respectively, confirming the profile shape as boxy ($R_{2.5} < 1.2$).

The dynamical mass of the DLA host can be roughly estimated as $M_{\text{dyn}} \sim (\Delta V^2 \times R)/G$, where ΔV is the characteristic velocity, and R the characteristic size. We will assume that the entire CO emission arises from a single object. A lower limit on its spatial extent can be obtained from the transverse separation between the optical and the blue CO components; the angular separation of $0''.9$ corresponds to a spatial separation of ≈ 6.5 kpc. Assuming $\Delta V \approx (W_{50}/\sin(48^\circ))/2 = 436 \text{ km s}^{-1}$ and $R \gtrsim 6.5$ kpc, we obtain $M_{\text{dyn}} \gtrsim 2.9 \times 10^{11} M_{\odot}$.

3.4 Results from the optical and near-IR data

The excellent spatial alignment between the CO emission map and the optical image of the candidate host galaxy in Fig. 3A, and the good agreement between the CO and the metal-line absorption and emission velocities in Sect. 3.2 clearly demonstrate that the CO $J=2-1$ emission originates in gas associated with the galaxy detected in the K -band and optical images. This constitutes the first case of spectroscopic identification of a DLA host galaxy via its molecular line emission. This is an important result in its own right, because it shows that ALMA has opened up a new window for the identification of DLA hosts, a task that has been fraught with much difficulty in the past. Of course, once the host has been identified via its molecular emission lines, additional data can be obtained and already existing data can be exploited, as has been done here.

Filter	Magnitude	Reference
u	24.89 ± 0.81	[1]
g	22.64 ± 0.22	[1]
r	21.90 ± 0.14	[1]
i	22.03 ± 0.23	[1]
$m_{11200 \text{ \AA}}$	20.20 ± 0.20	this work, Sect. 2.4.
$m_{13500 \text{ \AA}}$	19.90 ± 0.25	this work, Sect. 2.4.
K	19.16 ± 0.13	[2]

Table 3. The AB magnitudes of the $z = 0.7163$ galaxy, not corrected for Galactic reddening ($E_{B-V} = 0.024$, Schlafly & Finkbeiner (2011)). References: [1] Rao et al. (2011), [2] Hewett & Wild (2007).

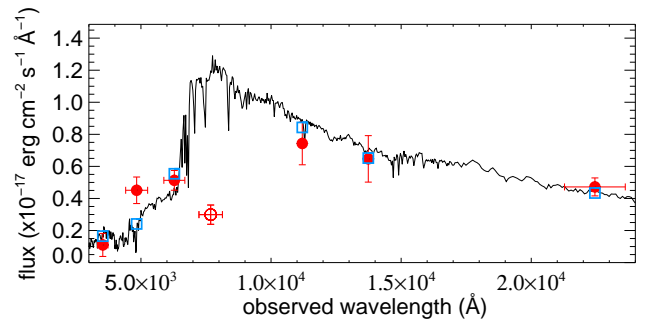


Figure 8. The best fit template fit to the galaxy’s SED is an instantaneous burst with an age of 0.5 Gyr, a metallicity that is 2.5 times the solar metallicity, and a reddening of $A_V = 0.4$ mag. The i -band shown by the outlined circle was not used in the fit because of large QSO subtraction residuals. The blue squares represent the expected flux, given the template model and the transmission curves of the different filters.

3.4.1 The stellar mass of the $z = 0.7163$ galaxy

To derive the stellar mass of the $z = 0.7163$ galaxy, we use the standard approach of fitting to the spectral energy distribution (SED), using release version 12.2 of HYPERZ (Bolzonella et al. 2000). We assume a Chabrier initial mass function (IMF), and derive different stellar masses, using templates with various star formation histories and metallicities between 0.2 and 2.5 times solar values (see Christensen et al. 2014, for further details).

The input photometry of the galaxy in $ugri$ filters is taken from Rao et al. (2011). However, strong residuals from the subtraction of the QSO’s point spread function have a strong effect on the i -band measurement (Rao et al. 2011)¹ and we hence choose to not include this band in the SED fit. The near-IR K -band data are from Hewett & Wild (2007), who obtained a magnitude similar to that obtained from the K -band adaptive optics data (Chun et al. 2010). In addition, we also use the magnitudes measured from our VLT-SINFONI data, derived in section 2.4. All photometric data are listed in Table 3.

We obtain a best-fit stellar mass of $\log[M_*/M_{\odot}] = 10.80^{+0.07}_{-0.14}$, as illustrated in Fig. 8, with a reddening of $A_V = 0.4^{+0.3}_{-0.3}$ mag, 2.5 times solar metallicity, and an age of ≈ 0.5 Gyr, assuming an instantaneous burst of star formation. To derive the 68% confidence intervals for the results, we assume a Gaussian error distribution, propagate the magnitude errors, and perform SED fits to 10^3 random realisations. Including the uncertain i -band data

¹ Images can be found at <http://enki.phyast.pitt.edu/Imaging.php>

point in the fit (shown as a red open circle in Fig. 8) significantly increases the χ^2 for the best fit, but yields a very similar derived stellar mass, $\log[M_*/M_\odot] = 10.94^{+0.05}_{-0.08}$.

3.4.2 Star formation rates

The galaxy has been previously suggested to be devoid of emission lines and most likely a 'red-and-dead' type. With our detection of multiple emission lines and 140 GHz continuum, we are now able to estimate the SFR using several tracers: the UV continuum emission, the [OII] and H α lines, but also the obscured SFR can be determined (see Sect. 3.4.3). We convert the measured flux densities and line fluxes to luminosities in the Λ CDM model adopted here, and then to SFRs, using the conversion factors in Kennicutt (1998). This calibration assumes a Salpeter IMF; a simple downward correction factor of 1.8 is finally used to shift to the assumption of a Chabrier IMF, for consistency with our SED fitting.

The u -band central transmission corresponds to a restframe wavelength of $\sim 2000\text{\AA}$ which implies an unobscured $\text{SFR}_{\text{UV}} = 0.43 \pm 0.23 M_\odot \text{ yr}^{-1}$. The large uncertainty reflects the large u -band magnitude error.

The [OII] emission line yields $\text{SFR}_{[\text{OII}]} = 0.51 \pm 0.05 M_\odot \text{ yr}^{-1}$, while the H α line yields $\text{SFR}_{\text{H}\alpha} = 1.6 \pm 0.4 M_\odot \text{ yr}^{-1}$. Apart from the fact that H α and [OII] trace SFRs on slightly different times scales, which could lead to this difference, we also stress that the H α emission is measured in a larger aperture than that used for the [OII] emission. In addition, the [OII] flux might be underestimated due to the non-photometric observing conditions and will be underestimated due to intrinsic extinction.

3.4.3 Dust mass, dust temperature and the obscured SFR

To determine the dust mass in the host galaxy, we use MAGPHYS (da Cunha et al. 2008) with the photometry in Table 3, the ALMA 140 GHz measurement of $53 \pm 17 \mu\text{Jy}$, and the Herschel photometry in Table 2, again fixing the redshift to that of the galaxy. MAGPHYS assumes a Chabrier IMF to generate galaxy templates, which makes the results directly comparable to the output of HYPERZ.

The Herschel resolution does not allow us to determine which fraction of the flux is from the DLA galaxy and which is from the QSO. In the higher resolution ALMA data we find that the relative fraction is 0.27/0.73, and in Sect. 2.2 we assumed the same ratio to hold for the Herschel data. Here we test this assumption. We proceed by forming a series of photometric tables where we split the Herschel flux 0.10/0.90, 0.20/0.80, ... 0.90/0.10 in steps of 0.10. For each table we derive the best fit model templates, and compute the combined χ^2 from the Herchel and ALMA data. The best fit is found where 0.30 of the Herschel flux comes from the DLA galaxy, supporting the assumption used in Sect. 2.2. With this assumption the maximum likelihood for the dust mass is found to be $\log[M_{\text{dust}}/M_\odot] = 8.45^{+0.10}_{-0.30}$, with a luminosity of $\log[L_{\text{dust}}/L_\odot] = 11.15 \pm 0.20$. The maximum likelihood peaks at a stellar mass of $\log[M_*/M_\odot] = 10.85 \pm 0.20$, in full agreement with our result in Sect. 3.4.1 ($10.80^{+0.07}_{-0.14}$). The fit yields an obscured SFR of $4.5^{+4.4}_{-2.6} M_\odot \text{ yr}^{-1}$ and a best fit dust temperature of $21.5 \pm 2 \text{ K}$ in the ambient interstellar medium.

In summary, the three optical/UV tracers yield low SFRs, in the range $\approx 0.4 - 1.6 M_\odot \text{ yr}^{-1}$. While the obscured SFR inferred from the fit to the dust emission is a little higher, it is still relatively low for a galaxy with this high stellar mass; its specific SFR is $= \text{SFR}/M_* \approx 10^{-11} \text{ yr}^{-1}$, which places it in the red sequence of

passively evolving galaxies in the correlation between SFRs and stellar masses (Wuyts et al. 2011).

3.4.4 Emission line metallicity

Having detected both H α and [NII] emission lines, we can use their line flux ratio $N2 = \log f([\text{NII}] 6584)/f(\text{H}\alpha)$ to infer the oxygen abundance of the host (e.g. Pettini & Pagel 2004; Kewley & Ellison 2008). We note that the relation between $N2$ and the metallicity is known to saturate at high metallicities (e.g. Steidel et al. 2014), and that one has to rely on extrapolations above solar metallicity (Pettini & Pagel 2004). Here, we use the calibration relation of Maiolino et al. (2008), which has been calibrated to higher-metallicity SDSS galaxies, using photoionization models (Kewley & Dopita 2002). Equally important, this calibration has been used to tie the conventional galaxy mass-metallicity relation (Tremonti et al. 2004) to the mass-metallicity relation in DLAs (Møller et al. 2013; Christensen et al. 2014).

From the $N2$ index, we infer $12+\log(\text{O}/\text{H}) = 9.20 \pm 0.09$. In addition to the measurement error, the $N2$ calibration itself has an intrinsic spread of ≈ 0.2 dex. The solar oxygen abundance is $12+\log(\text{O}/\text{H}) = 8.69$ (Asplund et al. 2009), yielding an oxygen metallicity of $[\text{O}/\text{H}] = +0.51 \pm 0.09$ (not including the calibration uncertainty), i.e. 3.2 times the solar value. This is in excellent agreement with both the independent result from the best fit SED model which had 2.5 times the solar value, and with the DLA absorption metallicity (Sect. 2.5).

4 DISCUSSION

In the vast array of possible techniques to select high- z galaxies (e.g. Lyman-break, Lyman- α emission, sub-mm emission, QSOs, ULIRGs, radio galaxies), the selection via damped Lyman- α absorption has always held a unique position. The use of absorption towards a background QSO implies that this selection is not subject to the usual luminosity bias that affects all emission-based methods, rather it is solely a function of the HI absorption cross-section. Consequently, some of the galaxies identified via the DLA approach may well not be identifiable by any other means; however, there does exist some overlap with traditional flux-limited samples, and this overlap allows one to use DLA samples to extend galaxy scaling relations out beyond the boundaries of emission-selected, flux-limited samples. Nevertheless, one of the critical questions in DLA studies has long been: "Is selection via damped Lyman- α absorption simply an alternative way to identify the same galaxies that are detected via flux-limited surveys, or does this selection also allow detection of galaxies that are missed in other surveys?". Several papers have addressed this question over the past decades considering all previously observable properties, but one important property, the molecular gas content, has so far not been possible to study for DLA galaxies. Now, with ALMA in operation, we are finally able to start filling in this missing section of parameter space.

Above we have reported the discovery of a CO line emitting galaxy (ALMA J132323.81-002154.1) at $z_{\text{CO}} = 0.71645$ and at the position of a known optical candidate DLA host. In this section we now compare the properties of this DLA galaxy to the properties of emission-selected galaxy samples. In particular, we ask if it lies within the range of the scaling relations known from flux-selected samples. Where possible, we also include our previous detection of the absorbing galaxy towards PKS 0439-433 = QSO J0441-4313 (Neeleman et al. 2016b). The HI column density of the absorber

Table 4. Physical parameters of the DLA host galaxy g1323. We provide parameters determined in this work and in addition parameters from the literature when relevant for the discussion of our new results.

Item	value	reference(s)
$\log[M_*/M_\odot]$	$10.80^{+0.07}_{-0.14}$	this work ³ , Sect. 3.4.1
$\log[M_{\text{mol-gas}}/M_\odot]$ †	10.37 ± 0.04	this work, Sect. 3.1
$\log[M_{\text{dyn}}/M_\odot]$	$\gtrsim 11.5$	this work, Sect. 3.3
$\log[M_{\text{dust}}/M_\odot]$	$8.45^{+0.10}_{-0.30}$	this work, Sect. 3.4.3
$\log[L_{\text{dust}}/L_\odot]$	11.15 ± 0.20	this work, Sect. 3.4.3
T_{dust}	21.5 ± 2 K	this work, Sect. 3.4.3
$z_{\text{abs } z\tau:50}$	0.71612	this work, Sect. 2.5
$z_{\text{abs } z\tau:\text{max}}$	0.71625	this work, Sect. 2.5
$z_{\text{em}} \text{ CO}(2-1)$	0.71645 ± 0.00009	this work, Sect. 3.3
$z_{\text{em}} \text{ [OII]}$	0.7170 ± 0.0006	this work, Sect. 2.3
$z_{\text{em}} \text{ H}\alpha$	0.7171 ± 0.0001	this work, Sect. 2.4
PA (<i>K</i> -band)	24.5°	a
PA (dust)	$(17 \pm 8)^\circ$	this work, Sect. 3.2.1
PA (CO)	$(32 \pm 14)^\circ$	this work, Sect. 3.2.1
PA (<i>J</i> -band)	$(29 \pm 7)^\circ$	this work, Sect. 2.4
PA (H α)	$(32 \pm 8)^\circ$	this work, Sect. 2.4
Impact parameter (<i>K</i> -band)	$1''.25 = 9.1$ kpc	a
Impact parameter (dust)	$1''.46 \pm 0''.2$	this work, Sect. 3.2.1
Impact parameter (CO)	$1''.03 \pm 0''.3$	this work, Sect. 3.2.1
Impact parameter (<i>J</i> -band)	$1''.3 \pm 0''.1$	this work, Sect. 2.4
Impact parameter (H α)	$1''.2 \pm 0''.1$	this work, Sect. 2.4
CO flux density	0.50 ± 0.05 Jy km s ⁻¹	this work, Sect. 3.1
[OII] flux	$2.8 \pm 0.3 \times 10^{-17}$ erg cm ⁻² s ⁻¹	this work ¹ , Sect. 2.3
H α flux	$12.0 \pm 3.9 \times 10^{-17}$ erg cm ⁻² s ⁻¹	this work, Sect. 2.4
[NII] $\lambda\lambda 6584$ flux	$5.6 \pm 1.8 \times 10^{-17}$ erg cm ⁻² s ⁻¹	this work, Sect. 2.4
W50 (CO line FWHM)	647 ± 54 km s ⁻¹	this work, Sect. 3.3
W20 (CO line)	652 ± 54 km s ⁻¹	this work, Sect. 3.3
inclination angle (<i>i</i>)	$40\text{--}48^\circ$	this work, Sect. 3.3
[OII] line FWHM	< 300 km s ⁻¹	this work, Sect. 2.3
H α line FWHM	238 ± 34 km s ⁻¹	this work ⁵ , Sect. 2.4
$\log[N(\text{H})/\text{cm}^{-2}]$	$20.21^{+0.21}_{-0.18}, 20.54^{+0.16}_{-0.15}$	b, c
Absorption metallicity, [Zn/H]	$0.61 \pm 0.20, 0.4 \pm 0.3$	d, Sect. 2.5
Galaxy abundance, $12+\log(\text{O}/\text{H})$	9.20 ± 0.09 ($\approx 3.2 \times$ solar)	this work, Sect. 3.4.4
Δv_{90}	141 ± 2 km s ⁻¹	this work, Sect. 2.5
SFR (UV)	$0.43 \pm 0.23 M_\odot \text{ yr}^{-1}$	this work, Sect. 3.4.2
SFR ([OII])	$0.51 \pm 0.05 M_\odot \text{ yr}^{-1}$	this work ² , Sect. 3.4.2
SFR (H α , SINFONI)	$1.6 \pm 0.4 M_\odot \text{ yr}^{-1}$	this work, Sect. 3.4.2
SFR (dust obscured)	$4.5^{+4.4}_{-2.6} M_\odot \text{ yr}^{-1}$	this work, Sect. 3.4.3
SFR (total)	$6.1^{+4.4}_{-2.6} M_\odot \text{ yr}^{-1}$	this work, Sect. 4.2
A_V	$0.4^{+0.3}_{-0.3}$	this work ³ , Sect. 3.4.1
$v_{\text{rel}}(\text{CO-abs})$	58 ± 16 km s ⁻¹	this work
$v_{\text{rel}}(\text{H}\alpha\text{-abs})$	171 ± 18 km s ⁻¹	this work, Sect. 2.5
R_e	4.0 kpc	a

† Assuming $\alpha_{\text{CO}} = 4.2 M_\odot (\text{K km s}^{-1} \text{ pc}^2)^{-1}$ and $r_{21} = 0.6$.

¹ Corrected for Galactic extinction, but not for intrinsic extinction in the galaxy. The FORS spectrum was obtained in non-photometric conditions, and slit losses are estimated to be $\approx 50\%$. A correction of at least a factor of two upwards is likely needed.

² Based on [OII] flux so notes above (under ¹) still apply. Assuming a Chabrier IMF.

³ Based on SED fit.

⁴ References: [a] Chun et al. (2010); [b] Rao et al. (2006); [c] Khare et al. (2004); [d] Péroux et al. (2006)

⁵ Corrected for resolution.

in PKS 0439-433 is below the classic definition of a DLA, but for simplicity we shall in what follows refer to both of the galaxies simply as “DLA galaxies” but keeping in mind the sub-DLA nature of the absorber towards PKS 0439.

4.1 The relation between molecular gas mass and stellar mass

Fig. 9 plots the molecular gas mass of the two absorbing galaxies versus their stellar mass, along with data from three comparison galaxy samples: COLD GASS, at $z \approx 0.02$ (Saintonge et al. 2011, in blue), ALLSMOG at $z \approx 0.04$ (Bothwell et al. 2014; Cicone et al. 2017, in red), and PHIBSS at $z \approx 1.2$ and ≈ 2.2 (Tacconi et al. 2013, in yellow). For convenience we use the same

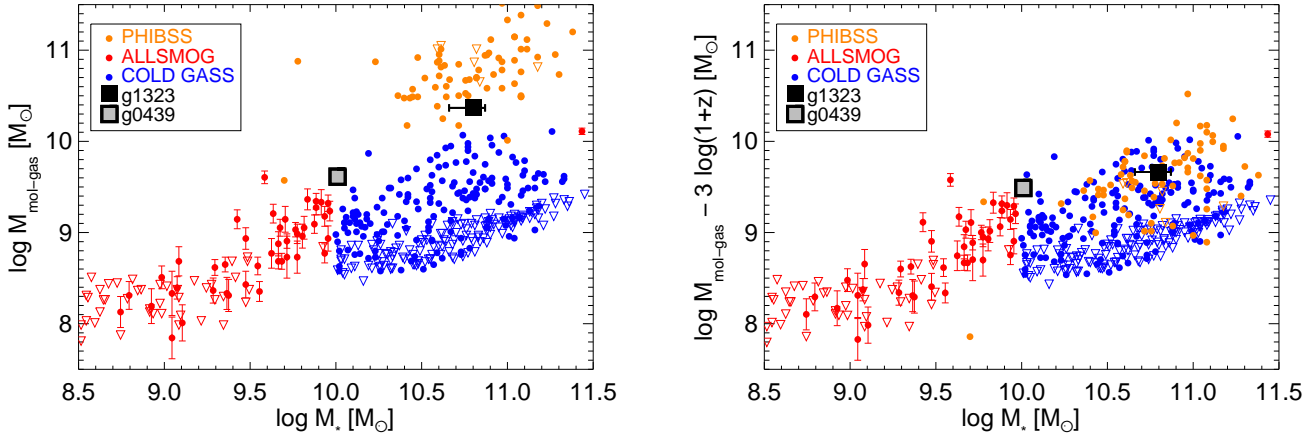


Figure 9. The molecular gas mass plotted against the stellar mass for the first two DLA galaxies detected in CO emission (redshifts 0.101 and 0.7163), compared to three literature samples: ALLSMOG, COLD GASS, and PHIBSS (at redshifts ≈ 0.02 , ≈ 0.04 , and ≈ 1.2 , 2.2 , respectively). The same CO-to-H₂ conversion factor, $\alpha_{\text{CO}} = 4.2 \text{ M}_{\odot} (\text{K km s}^{-1} \text{ pc}^2)^{-1}$, was used for all galaxies in both panels. Upper limits on $M(\text{H}_2)$ are indicated by open triangles pointing down. In the left panel, no correction has been applied for the redshift evolution of the relation between molecular gas mass and stellar mass; in the right panel, a redshift correction of $(1+z)^{-3}$ has been applied to the molecular gas mass. See text for discussion.

Table 5. Properties of g0439

Item	value	reference
$\log[M_*/M_{\odot}]$	10.01 ± 0.02	a
$\log[M_{\text{mol-gas}}/M_{\odot}]$	9.60 ± 0.1	b
W50 (CO line FWHM)	$283 \pm 21 \text{ km s}^{-1}$	c
W20 (CO line)	$285 \pm 21 \text{ km s}^{-1}$	c
inclination angle (i)	67^{+6}_{-5} deg	b

[a] Christensen et al. 2014; [b] Neeleman et al. 2016b; [c] this work.

CO-to-H₂ conversion factor, $\alpha_{\text{CO}} = 4.2 \text{ M}_{\odot} (\text{K km s}^{-1} \text{ pc}^2)^{-1}$ for all galaxies in the figure. The left panel shows that the COLD GASS and ALLSMOG samples lie on the well-known correlation between molecular gas mass and stellar mass. Conversely, the two absorbers lie at or above the upper boundary of this wide relation. For easy reference in this figure, and in the remainder of the paper, we use the short-hand notation g0439 and g1323 for the two galaxies. In Table 4, we list the known properties of g1323; Table 5 provides a summary of the relevant properties of g0439.

Galaxies from the PHIBSS sample are seen to have systematically larger gas masses than the two absorbers, as well as than the flux selected samples in the nearby Universe. However, to obtain a fair comparison between the galaxies at different redshifts, we must take the redshift evolution of this scaling relation into account. The simplest view is that the relation between molecular gas mass and stellar mass scales (empirically) as $(1+z)^{-3}$ between redshifts 0 and 2.5 (Genzel et al. 2015); this empirical correction is applied in the right panel of Fig. 9. The figure shows that the high- z PHIBSS points have now moved down to perfectly overlap with the two low- z galaxy samples. The two absorbers remain in the upper part of the distribution, but now lie within the spread of the distribution of the emission-selected galaxies. We note that both absorbers appear to be rich in molecular gas; notably, g0439 lies on the upper boundary of the distribution.

4.2 The SFR, molecular gas fraction, and stellar mass relations

The other view on the influence of redshift on scaling relations is that of “fundamental relation invariance”. In this view, the values of physical parameters describing the galaxies are tied to each other to only allow galaxies to fill small sub-sets of physical parameter space, and galaxy samples then “drift” through this parameter space, yielding an apparent redshift evolution in individual parameters. Santini et al. (2014) formulated such a fundamental relation between the SFR, the gas fraction ($f_{\text{gas}} = M_{\text{gas}}/(M_* + M_{\text{gas}})$, where M_{gas} is the total gas mass), and the stellar mass, with the claim that all galaxies, at all redshifts (out to $z \approx 2.5$, the upper limit of the redshifts of the galaxies of their sample), must lie on this relation. In order to test if a similar relation exists for molecular gas mass alone ($f_{\text{mol-gas}} = M_{\text{mol-gas}}/(M_* + M_{\text{mol-gas}})$), and in particular to test if g1323 then lies on this relation, we first use the same comparison samples as above, but now cut out a thin slice in stellar mass of each sample, centred on the M_* of g1323. In figures 10 and 11 we plot SFR vs $f_{\text{mol-gas}}$ of galaxies within the mass range $10^{10.6} \leq M_*/M_{\odot} \leq 10^{11.0}$. Several different indicators for the SFR are available, applicable at various wavelengths, and in order to provide appropriate and unbiased comparisons we use different symbols for UV- and H α -based SFR in Fig. 10, while total SFRs corrected for the dust obscured component are plotted in Fig. 11. For comparison we also plot the relevant total gas mass relations within which the galaxies should lie (computed from equation 9 and Table 1 of Santini et al. 2014). For completeness we note here that the calibration of the relation as parameterised by Santini et al. (2014) is based on a Salpeter IMF. For an internally consistent comparison, we have converted their SFR values to a Chabrier IMF, by subtracting 0.24 dex from their reported $\log[M_*/M_{\odot}]$ and 0.15 dex from their $\log[\text{SFR}]$.

In order to obtain SFRs for the three comparison samples we proceeded as follows. COLD GASS galaxies were cross-matched with the SDSS database, and H α -based SFRs were ex-

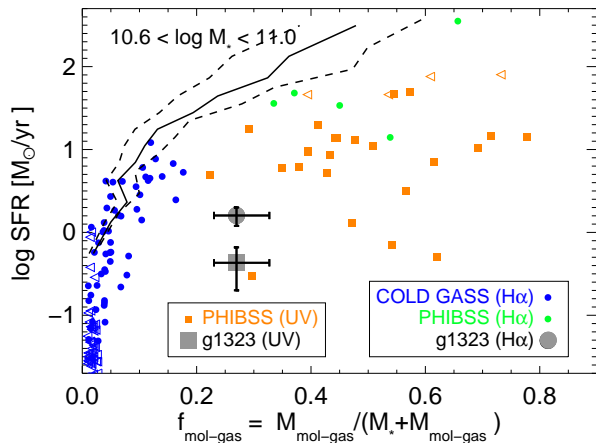


Figure 10. SFR vs molecular gas fraction $f_{\text{mol-gas}} = M_{\text{mol-gas}}/(M_{\text{mol-gas}} + M_*)$. Following the fundamental relation between M_* , f_{gas} and SFR we plot only galaxies in a narrow stellar mass range centred at $\log[M_*/M_\odot] = 10.80$ (full curve), with the mass range $10^{10.6} \leq M_*/M_\odot \leq 10^{11.0}$ (dashed curves). We plot UV- and H α -based SFRs with different symbols. Orange squares mark $z \approx 1.2$ UV-based SFR, green circles mark $z \approx 2.2$ H α -based SFR determinations. Triangles pointing to the left are upper detection limits on $f_{\text{mol-gas}}$.

tracted from aperture corrected SFRs (Brinchmann et al. 2004)². For ALLSMOG galaxies Ciccone et al. (2017) (ALLSMOG website³) list the SFRs (again H α and based on SDSS database values), and we also obtained H α -based SFRs for part of the PHIBSS sample from Erb et al. (2006). For the remaining galaxies in the COSMOS and GOODS-N fields we obtained estimates of the UV SFRs from the Rainbow database⁴, which reports the UV-based SFRs derived from SED fits with FAST (Kriek et al. 2009). Tacconi et al. (2013) report a total SFR from either extinction corrected H α emission (filled green circles in Fig. 11), or from the sum of UV- and IR-based SFRs (filled yellow circles in Fig. 11). The systematic uncertainties are reported to be ± 0.15 dex. We compute the total SFR of g1323 by adding our H α -based SFR and the dust obscured SFR and find $\text{SFR}_{\text{total}} = 6.1^{+4.4}_{-2.6} M_\odot \text{ yr}^{-1}$.

From Fig. 10 we first note that the UV-based SFRs (square symbols) all fall far below the relation, and that g1323 is in the very low range of this wide distribution. Considering now only the H α -based SFRs (filled circles), they are all seen to lie closer to the relation, and are likely much better SFR indicators for galaxies with large molecular gas mass fractions. It is seen that most points fall well below the corresponding relation for total gas mass, and increasingly so for larger gas mass fractions. Still, even for $f_{\text{mol-gas}}$ as large as 0.4-0.5 the PHIBSS galaxies fall only marginally below the relation. In contrast, the H α -based SFR of g1323 falls significantly below it (note that the flux-based uncertainty is linear in SFR, but we are plotting $\log(\text{SFR})$ in the figures). While g1323 obviously has a large $f_{\text{mol-gas}}$ compared to the COLD GASS galaxies, it is still surprising that it falls so far below the relation followed by the low $f_{\text{mol-gas}}$ galaxies, and even far below the PHIBSS galaxies that have larger $f_{\text{mol-gas}}$. Either g1323 could have an even

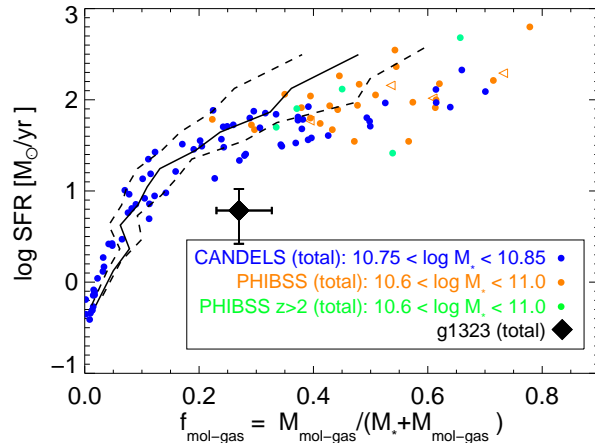


Figure 11. Same as Fig. 10 but here we plot total SFR. Again the orange and green dots are objects from the PHIBSS survey while the black lines mark the fundamental relation shown in Fig. 10. For COLD GASS we do not have total SFRs and instead we plot in blue galaxies from the CANDELS sample in a very narrow stellar mass range $10^{10.75} \leq M_*/M_\odot \leq 10^{10.85}$. The flux limited samples are seen to follow a relation similar to that previously found for total gas mass (black curve), but shifted increasingly to the right for larger $f_{\text{mol-gas}}$. g1323 is again seen to have a very low SFR for a galaxy with its stellar mass and large molecular gas mass fraction.

larger hidden SFR than the PHIBSS galaxies, or it simply has an extremely low SFR for its stellar mass and gas fraction.

To find out which is true, we therefore plot, in Fig. 11, the “total SFR” corrected for dust. We do not have the information to compute the dust correction for the COLD GASS galaxies but total SFRs are available for both sub-samples of the PHIBSS galaxies. The corrected PHIBSS sample is seen now to lie closer to the Santini et al. (2014) relation but it still lies somewhat below and with a scatter slightly larger than the mass slice would predict. In order to obtain a better evaluation of how the relation based on $f_{\text{mol-gas}}$ compares to that of the total gas mass relation, we also include CANDELS galaxies from Popping et al. (2015) for which total SFRs are also known. The molecular gas mass for the CANDELS galaxies has not been measured, rather it has been inferred from a suite of optical data and the model presented in Popping et al. (2015). It is seen that for $f_{\text{mol-gas}} < 0.2$ the CANDELS sample follows the Santini et al. (2014) relation well, whereas it for larger $f_{\text{mol-gas}}$ connects perfectly with the PHIBSS sample. The CANDELS sample is very large allowing us to select an even narrower mass slice ($10^{10.75} \leq M_*/M_\odot \leq 10^{10.85}$) than for PHIBSS. While care must be exercised in not over interpreting the partly model based CANDELS data points, the general trend of the relation from small to large $f_{\text{mol-gas}}$ appears now to be well established. The scatter of the CANDELS sample is seen to be smaller than for the PHIBSS sample, which was expected because the CANDELS galaxies are picked from a narrower mass range. g1323 is again seen to fall well below both samples. We conclude this discussion summarising our two main results: (i) there is indeed a fundamental relation for $(f_{\text{mol-gas}}, \text{SFR}, M_*)$ similar to that of total gas mass fraction but shifted a little towards larger $f_{\text{mol-gas}}$ and, (ii) g1323 lies well below this relation. It therefore appears that g1323, seen in this observed parameter space and stellar mass range, does not have counterparts in flux-selected samples. It is noteworthy that Neeleman et al. (2016b) reported a low SFR and large gas consumption timescale for g0439.

² SFRs are obtained from the JHU-MPA value-added catalog https://www.sdss3.org/dr9/algorithms/galaxy_mpa_jhu.php

³ <http://www.mrao.cam.ac.uk/ALLSMOG/>

⁴ https://rainbowx.fis.ucm.es/Rainbow_Database/Home.html

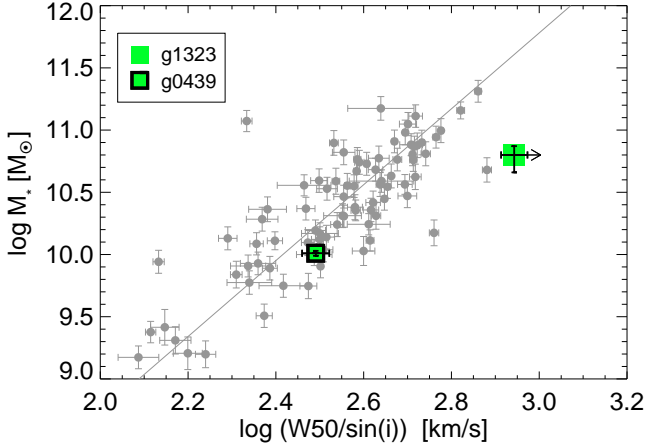


Figure 12. Comparison to the CO-Tully-Fisher relation of the COLD GASS sample from Tiley et al. (2016) (small grey dots). For g1323 we have used the conservative estimate $i = 48^\circ$ (Sect. 3.3). The inclination could be smaller, and the arrow marks where it would move for an inclination of e.g. $i = 40^\circ$.

There are ways to apply reasonable assumptions to force g1323 onto the relation of course, but before we turn to those we emphasize that such assumptions have also not been applied to any of the objects of the comparison samples, so at face value, with the zero'th order assumptions, g1323 is significantly inconsistent, both considering $H\alpha$ -based and total SFR, with the relation of the flux-selected samples.

For g1323 we found (Sect. 3.4.3) that there is indeed evidence for some obscured SFR (as included in Fig. 11). One could hypothesize that even more SFR is hidden by dust, thereby pushing the point further upwards towards the relation. This hypothesis is not supported by the data analyzed in Sect. 3.4.3. Alternatively one could assume a lower value for α_{CO} for g1323, which would push the point towards the left. Assuming e.g. the extreme example (Sect. 3.1) of a starburst galaxy, with $\alpha_{CO} \approx 1$ and $r_{21} \approx 1$, would imply $f_{mol-gas} = 0.05$. The assumption of such a highly obscured starburst is also not supported by our observations, as described in Sect. 4.4.

4.3 CO-Tully-Fisher relation

In Fig. 12 we compare our absorbing galaxies to the COLD GASS Tully-Fisher relation (figure 2b in Tiley et al. 2016). For g0439 we fit the same double-horned profile as for g1323 (Sect. 3.3) and find the values for W50 and W20 listed in Table 5. Both galaxies are seen to fall to the right of the relation (i.e. they have large velocity widths for their stellar masses). g0439 is fully consistent with the scatter of the COLD GASS sample, but g1323 is seen to fall significantly right of the relation.

As discussed in Sect. 3.2 there is some evidence that part of the CO line profile (the lowest redshift peak) may be due to a gas component which is separate from the rest of the galaxy. If we instead use $W50 = 378 \text{ km s}^{-1}$ from the “two object fit” (Sect. 3.3) then the green square moves left by 0.23 dex in Fig. 12, which brings it in agreement with the COLD GASS distribution. The “outlier” nature of g1323 in the TF relation would therefore find a simple explanation if the existence of this separate component is confirmed.

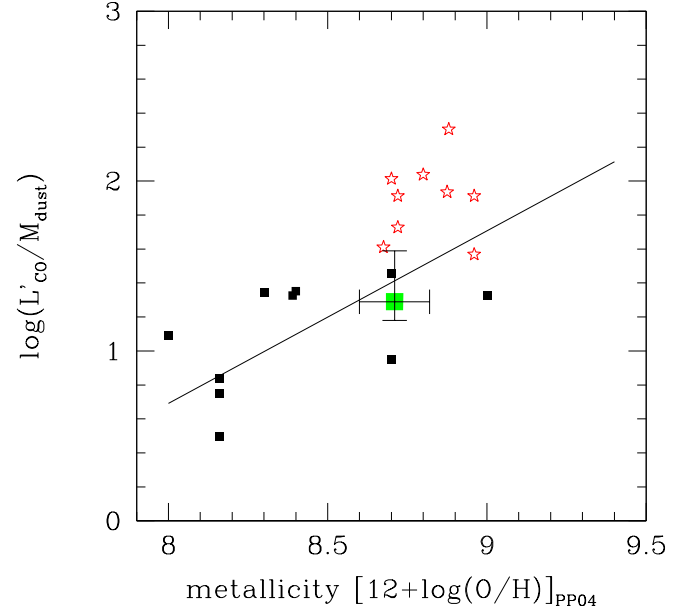


Figure 13. Gas-to-dust vs metallicity relation for local group galaxies (small black squares) and local ULIRGs (red stars). g1323 (large green square) is seen to lie well within the parameter space of local group galaxies of similar metallicity (adapted from Magdis et al. (2011)).

4.4 Gas-to-dust mass vs metallicity relation

For local galaxies it is known that the ratio of gas to dust mass is related to the emission line metallicity of the galaxy. We did not detect any dust emission continuum in our ALMA data of g0439, but for g1323 we obtained a detection and inferred a dust mass of $\log[M_{dust}/M_\odot] = 8.45^{+0.10}_{-0.30}$ (Sect. 3.4.3). In Fig. 13 we now compare g1323 (large green square) to the sample of local group galaxies (small black squares) and local ULIRGs (red stars) compiled in Magdis et al. (2011). In order to compare to the Magdis et al. (2011) sample we need to first convert our measured emission line metallicity to the calibration by Pettini & Pagel (2004) and we find $[12 + \log(O/H)]_{PP04} = 8.71 \pm 0.11$. As Magdis et al. (2011) (their Figure 3, right) we plot L'_{CO} rather than M_{gas} in order to avoid the additional uncertainty arising from α_{CO} .

From Fig. 13 we first conclude that g1323 is lying perfectly on this scaling relation for normal flux-selected galaxies. While it is marginally consistent with the position of ULIRGs, the fit to the relation of local galaxies (black line) is much better, a conclusion which is also supported by our result in Sect. 3.4.3 that this galaxy has a relatively low amount of obscured SFR for its stellar mass, as well as only modest reddening ($A_V = 0.4$, Sect. 3.4.1).

4.5 Relation to emission-selected galaxy samples

DLA galaxies make up a sample of galaxies that are almost exclusively first identified in absorption (i.e. absorption-selected). This is an important characteristic to keep in mind, because it means that we do not a priori know if “absorption selection” is a differently weighted process to find the same galaxies as “flux-limited selection”, or if it is a way of finding entirely different objects. This question is not easily answered, and yet it is of fundamen-

tal importance in order to be able to correctly interpret flux-limited galaxy samples, and in particular to be able to connect them to the vast reservoir of information gathered via absorption line studies of DLAs. Finding the answer requires that we identify a sample of DLA galaxies in emission, and then that we carry out a detailed study to test if those objects lie within the same parameter space as emission selected galaxies.

Møller et al. (2002) and Weatherley et al. (2005) previously addressed this exact question using a small set of $z = 2-3$ DLA galaxies observed in optical and NIR emission. The conclusion at that time was that all the measured emission properties were consistent with the conjecture that DLA galaxies are Lyman Break Galaxies. One of the key purposes of our ALMA survey is now to extend this fundamental test into the ALMA frequency range, where we are able to ask the same question for properties related to the molecular gas. In this paper we have outlined this procedure, and compared our first two detections to galaxy gas scaling relations determined from flux limited samples. Here we provide a short summary of this comparison.

- **M_{gas} vs M_* :** both galaxies are rich in molecular gas; notably, g0439 lies on the upper boundary of the known distribution. Both are within the parameter space of flux limited samples.

- **SFR vs molecular gas fraction:** Neeleman et al. (2016b) reported a low SFR and large gas consumption timescale for g0439. Similarly we have here found that the SFR of g1323 is significantly below the flux limited relation for galaxies of similar stellar mass and molecular gas-mass fraction, both considering purely $H\alpha$ -based SFRs, and total (dust corrected) SFRs.

- **Tully-Fisher relation:** the two galaxies have a large CO line velocity width for their stellar mass. g0439 is here within the standard relation of the COLD GASS sample, but g1323 is also in this respect at best marginally within the flux limited relation.

- **Gas-to-dust vs metallicity:** we were only able to obtain a dust mass of g1323. This galaxy lies directly on the known relation of normal (i.e. non starburst) main sequence galaxies.

The answer is therefore not as clear as it was in the earlier works where only stellar and ionized gas components were considered. g1323 appears to be the first case of a DLA-selected galaxy that does not have counterparts in flux-limited samples as it fails our consistency test in two out of four relations. This galaxy may simply be a very unique and rare case, but it may in fact represent an “in between burst”, or “post starburst” low SFR phase of galactic evolution. If such a phase follows an event of strong ejection of gas (both molecular and neutral), then the ejected molecular kinematic component could explain the large CO emission line width, and also explain why galaxies in such a phase are more easily found as DLA galaxies due to their larger cross section for HI absorption.

Some support for this interpretation may be found in our detailed analysis of the ALMA data presented here which suggests that (i) g1323 consists of two kinematically independent and interacting sub-clouds and (ii) the SED fit to g1323 favours an instantaneous burst of starformation with an age of 0.5 Gyr. The current data do not rule out the possibility that both clouds may have a stellar component, but only one of them is visible on the current (ground based AO) optical image. An HST image should be able to determine if the additional cloud belongs to a separate and interacting galaxy.

A key conclusion from our previous study was that “the strongest molecular absorption component of g0439 cannot arise from the molecular disk” (Neeleman et al. 2016b) suggesting that also that system has more than one molecular gas component. A

larger sample must be collected in order to address how common this type of objects are in DLA selected samples. Our Cycle 3 data are currently being analyzed and they will already significantly enlarge our current sample of detections (Kanekar et al. in prep).

5 SUMMARY AND CONCLUSIONS

We have initiated an ALMA survey for CO emission from galaxies known to harbour DLA or sub-DLA absorbers. In this paper we present an ALMA map of the field around the known DLA absorber towards the quasar J1323–0021. Based on the detection of CO(2-1) line emission at a redshift of $z_{CO} = 0.71645$, close to that of the absorber ($z_{abs} = 0.71625$), we identify the galaxy responsible for the absorption. This is the second DLA/sub-DLA galaxy in which CO emission has been detected, and it is the highest redshift DLA CO detection to date. This is also the first case of a DLA galaxy identified via molecular gas emission, and as such it highlights a new and promising route to the identification of DLA galaxies. With ALMA we also detect the dust continuum and therefore measure both the molecular and the dust mass of the host galaxy.

In addition we present new VLT-FORS2 data and we re-analyze archival VLT SINFONI data cubes, Herschel maps, and VLT UVES and HST STIS spectra. This large suite of data allows us to dissect the DLA host galaxy in terms of stellar mass, gas mass and dust mass; and in terms of kinematical components of the cold (CO) gas, the ionized ($H\alpha$ and [OII]) gas and the absorbing gas. Also, we are able to determine the SFR using several different indicators (UV, [OII], $H\alpha$ and IR).

Our results can be summarized as follows:

- The DLA galaxy g1323 is the second most massive DLA-selected galaxy known with $\log[M_*/M_\odot] = 10.80^{+0.07}_{-0.14}$, $\log[M_{mol-gas}/M_\odot] = 10.37 \pm 0.04$ and $\log[M_{dust}/M_\odot] = 8.45^{+0.10}_{-0.30}$. This also implies that it is very gas rich, in the upper part of comparable galaxies from flux limited samples.

- The emission line metallicity of g1323 is super solar ($\approx 3.2 \times$ solar), fully consistent with previously published absorption metallicities. Its gas-to-dust ratio for this metallicity is perfectly on the relation for normal flux selected galaxies. It is somewhat below, but within the errors also marginally consistent with local ULIRGs.

- The velocity width of the CO emission is extremely wide for its stellar mass. It falls outside the scatter of the CO-Tully-Fisher relation of COLD GASS galaxies. There is some evidence suggesting that the wide CO line could be due to an additional and separate (both dynamically and spatially), interacting CO cloud, e.g. a previous outflow or/and current infall. This cloud could also be related to a separately, yet undiscovered, interacting galaxy.

- We determine the SFR in several different ways and find that for a galaxy with its stellar mass and molecular gas-mass fraction, its SFR is extremely low. With respect to its poor ability to convert molecular gas into stars this galaxy has no counterparts in flux limited samples. It is intriguing that a low SFR and large gas consumption timescale was also found for our first CO-detected absorber.

As in previous (but optically based) studies we perform the fundamental test if the properties of g1323 are consistent with the conjecture that DLA-selected galaxies and flux-selected galaxies are the same, only selected in different ways. We find that for the first time we have identified a DLA galaxy that does not appear to have counterparts in flux limited samples. The galaxy g1323 has too low SFR for a galaxy with its stellar mass and gas-mass fraction,

and it also has too wide a CO emission line to fit onto the well known Tully-Fisher relation.

Our survey is ongoing, and our Cycle 3 data have already provided additional detections. If more DLA galaxies of this survey in similar ways do not conform to the relations of emission selected samples, this could have significant impact on our understanding of the connection between the gaseous and the stellar component of galaxies, and how they relate to starformation. Notably the non-disk molecular gas component of DLA galaxies could form a large previously unexplored reservoir.

ACKNOWLEDGEMENTS

We are grateful to Mark R. Chun for providing the AO *K*-band image, to Gergely Popping for providing the unpublished CANDELS molecular masses, and to Giorgos Magdis and Celine Peroux for useful discussions. JPUF acknowledges support from the ERC-StG grant EGG5-278202. LC and HR are supported by YDUN-DFF grant ID 4090-00079. NK acknowledges support from the Department of Science and Technology via a Swarnajayanti Fellowship (DST/SJF/PSA-01/2012-13). This paper makes use of the following ALMA data: ADS/JAO.ALMA#2013.1.01178.S. ALMA is a partnership of ESO (representing its member states), NSF (USA) and NINS (Japan), together with NRC (Canada), NSC and ASIAA (Taiwan), and KASI (Republic of Korea), in cooperation with the Republic of Chile. The Joint ALMA Observatory is operated by ESO, AUI/NRAO and NAOJ. This work has made use of the Rainbow Cosmological Surveys Database, which is operated by the Universidad Complutense de Madrid (UCM), partnered with the University of California Observatories at Santa Cruz (UCO/Lick,UCSC).

REFERENCES

- Asplund, M., Grevesse, N., Sauval, A. J., & Scott, P., 2009, *ARA&A*, 47, 481
- Battisti, A. J., Meiring, J. D., Tripp, T. M., et al., 2012, *ApJ*, 744, 93
- Bolatto, A. D., Wolfire, M., & Leroy, A. K., 2013, *ARA&A*, 51, 207
- Bolzonella, M., Miralles, J.-M., & Pelló, R., 2000, *A&A*, 363, 476
- Bothwell, M. S., Wagg, J., Cicone, C., et al., 2014, *MNRAS*, 445, 2599
- Bouché, N., Murphy, M. T., Péroux, C., et al., 2012, *MNRAS*, 419, 2
- Bowen, D. V., Huchtmeier, W., Brinks, E., Tripp, T. M., & Jenkins, E. B., 2001, *A&A*, 372, 820
- Briggs, F. H. & Barnes, D. G., 2006, *ApJ*, 640, L127
- Briggs, F. H., de Bruyn, A. G., & Vermeulen, R. C., 2001, *A&A*, 373, 113
- Brinchmann, J., Charlot, S., White, S. D. M., Tremonti, C., Kauffmann, G., Heckman, T., & Brinkmann, J., 2004, *MNRAS*, 351, 1151
- Carilli, C. L. & Walter, F., 2013, *ARA&A*, 51, 106
- Charlot, S. & Fall, S. M., 1991, *ApJ*, 378, 471
- Chen, H.-W. & Lanzetta, K. M., 2003, *ApJ*, 597, 706
- Chengalur, J. N., Ghosh, T., Salter, C. J., Kanekar, N., Momjian, E., Keeney, B. A., & Stocke, J. T., 2015, *MNRAS*, 453, 3135
- Chengalur, J. N. & Kanekar, N., 2002, *A&A*, 388, 383
- Christensen, L., Møller, P., Fynbo, J. P. U., & Zafar, T., 2014, *MNRAS*, 445, 225
- Christensen, L., Noterdaeme, P., Petitjean, P., Ledoux, C., & Fynbo, J. P. U., 2009, *A&A*, 505, 1007
- Chun, M. R., Gharanfoli, S., Kulkarni, V. P., & Takamiya, M., 2006, *AJ*, 131, 686
- Chun, M. R., Kulkarni, V. P., Gharanfoli, S., & Takamiya, M., 2010, *AJ*, 139, 296
- Cicone, C., Bothwell, M., Wagg, J., et al., 2017, *A&A*, 604, A53
- Colbert, J. W. & Malkan, M. A., 2002, *ApJ*, 566, 51
- Cooke, R., Pettini, M., Steidel, C. C., King, L. J., Rudie, G. C., & Rakic, O., 2010, *MNRAS*, 409, 679
- da Cunha, E., Charlot, S., & Elbaz, D., 2008, *MNRAS*, 388, 1595
- Danielson, A. L. R., Swinbank, A. M., Smail, I., et al., 2011, *MNRAS*, 410, 1687
- Dannerbauer, H., Daddi, E., Riechers, D. A., Walter, F., Carilli, C. L., Dickinson, M., Elbaz, D., & Morrison, G. E., 2009, *ApJ*, 698, L178
- Davis, T. A., Bureau, M., Young, L. M., et al., 2011, *MNRAS*, 414, 968
- Ellison, S. L., Hennawi, J. F., Martin, C. L., & Sommer-Larsen, J., 2007, *MNRAS*, 378, 801
- Erb, D. K., Steidel, C. C., Shapley, A. E., Pettini, M., Reddy, N. A., & Adelberger, K. L., 2006, *ApJ*, 647, 128
- Fixsen, D. J., Bennett, C. L., & Mather, J. C., 1999, *ApJ*, 526, 207
- Fumagalli, M., O’Meara, J. M., Prochaska, J. X., Kanekar, N., & Wolfe, A. M., 2014, *MNRAS*, 444, 1282
- Fumagalli, M., O’Meara, J. M., Prochaska, J. X., Rafelski, M., & Kanekar, N., 2015, *MNRAS*, 446, 3178
- Fynbo, J. P. U., Geier, S. J., Christensen, L., et al., 2013, *MNRAS*, 436, 361
- Fynbo, J. P. U., Laursen, P., Ledoux, C., et al., 2010, *MNRAS*, 408, 2128
- Fynbo, J. P. U., Ledoux, C., Noterdaeme, P., et al., 2011, *MNRAS*, 413, 2481
- Fynbo, J. P. U., Prochaska, J. X., Sommer-Larsen, J., Dessauges-Zavadsky, M., & Møller, P., 2008, *ApJ*, 683, 321
- Fynbo, J. U., Møller, P., & Warren, S. J., 1999, *MNRAS*, 305, 849
- Genzel, R., Tacconi, L. J., Lutz, D., et al., 2015, *ApJ*, 800, 20
- Griffin, M. J., Abergel, A., Abreu, A., et al., 2010, *A&A*, 518, L3
- Guillemin, P. & Bergeron, J., 1997, *A&A*, 328, 499
- Haehnelt, M. G., Steinmetz, M., & Rauch, M., 1998, *ApJ*, 495, 64
- Hartoog, O. E., Fynbo, J. P. U., Kaper, L., De Cia, A., & Bagdonaitė, J., 2015, *MNRAS*, 447, 2738
- Hewett, P. C. & Wild, V., 2007, *MNRAS*, 379, 738
- Jorgenson, R. A. & Wolfe, A. M., 2014, *ApJ*, 785, 16
- Kanekar, N., Athreya, R. M., & Chengalur, J. N., 2002, *A&A*, 382, 838
- Kanekar, N. & Briggs, F. H., 2004, *New Astr. Rev.*, 48, 1259
- Kanekar, N. & Chengalur, J. N., 2003, *A&A*, 399, 857
- , 2005, *A&A*, 429, L51
- Kanekar, N., Chengalur, J. N., Subrahmanyam, R., & Petitjean, P., 2001, *A&A*, 367, 46
- Kanekar, N., Prochaska, J. X., Smette, A., et al., 2014, *MNRAS*, 438, 2131
- Kanekar, N., Smette, A., Briggs, F. H., & Chengalur, J. N., 2009, *ApJ*, 705, L40
- Kennicutt, Jr., R. C., 1998, *ARA&A*, 36, 189
- Kewley, L. J. & Dopita, M. A., 2002, *ApJS*, 142, 35
- Kewley, L. J. & Ellison, S. L., 2008, *ApJ*, 681, 1183
- Khare, P., Kulkarni, V. P., Lauroesch, J. T., York, D. G., Crofts, A. P. S., & Nakamura, O., 2004, *ApJ*, 616, 86

- Komatsu, E. & et al., 2011, *ApJS*, 192, 18
- Krogager, J.-K., Fynbo, J. P. U., Ledoux, C., et al., 2013, *MNRAS*, 433, 3091
- Krogager, J.-K., Fynbo, J. P. U., Møller, P., Ledoux, C., Noterdaeme, P., Christensen, L., Milvang-Jensen, B., & Sparre, M., 2012, *MNRAS*, 424, L1
- Krogager, J.-K., Møller, P., Fynbo, J. P. U., & Noterdaeme, P., 2017, *MNRAS*, 469, 2959
- Kulkarni, V. P., Fall, S. M., Lauroesch, J. T., York, D. G., Welty, D. E., Khare, P., & Truran, J. W., 2005, *ApJ*, 618, 68
- Kulkarni, V. P., Woodgate, B. E., York, D. G., Thatte, D. G., Meiring, J., Palunas, P., & Wassell, E., 2006, *ApJ*, 636, 30
- Lacy, M., Becker, R. H., Storrie-Lombardi, L. J., Gregg, M. D., Urrutia, T., & White, R. L., 2003, *AJ*, 126, 2230
- Lanzetta, K. M., Wolfe, A. M., Altan, H., et al., 1997, *AJ*, 114, 1337
- Le Brun, V., Bergeron, J., Boisse, P., & Deharveng, J. M., 1997, *A&A*, 321, 733
- Ledoux, C., Petitjean, P., Fynbo, J. P. U., Møller, P., & Srianand, R., 2006, *A&A*, 457, 71
- Leroy, A. K., Bolatto, A., Gordon, K., et al., 2011, *ApJ*, 737, 12
- Lowenthal, J. D., Hogan, C. J., Green, R. F., Woodgate, B., Caulet, A., Brown, L., & Bechtold, J., 1995, *ApJ*, 451, 484
- Lowrance, J. L., Morton, D. C., Zucchini, P., Oke, J. B., & Schmidt, M., 1972, *ApJ*, 171, 233
- Magdis, G. E., Daddi, E., Elbaz, D., et al., 2011, *ApJ*, 740, L15
- Maiolino, R., Nagao, T., Grazian, A., et al., 2008, *A&A*, 488, 463
- Mazumdar, P., Kanekar, N., & Prochaska, J. X., 2014, *MNRAS*, 443, L29
- Møller, P., Fynbo, J. P. U., & Fall, S. M., 2004, *A&A*, 422, L33
- Møller, P., Fynbo, J. P. U., Ledoux, C., & Nilsson, K. K., 2013, *MNRAS*, 430, 2680
- Møller, P. & Warren, S. J., 1993, *A&A*, 270, 43
- Møller, P., Warren, S. J., Fall, S. M., Fynbo, J. U., & Jakobsen, P., 2002, *ApJ*, 574, 51
- Monier, E. M., Turnshek, D. A., & Rao, S., 2009, *MNRAS*, 397, 943
- Neeleman, M., Kanekar, N., Prochaska, J. X., Rafelski, M., Carilli, C. L., & Wolfe, A. M., 2017, *Science*, 355, 1285
- Neeleman, M., Prochaska, J. X., Ribaud, J., Lehner, N., Howk, J. C., Rafelski, M., & Kanekar, N., 2016a, *ApJ*, 818, 113
- Neeleman, M., Prochaska, J. X., Zwaan, M. A., et al., 2016b, *ApJ*, 820, L39
- Neeleman, M., Wolfe, A. M., Prochaska, J. X., & Rafelski, M., 2013, *ApJ*, 769, 54
- Noterdaeme, P., Laursen, P., Petitjean, P., et al., 2012a, *A&A*, 540, 63
- Noterdaeme, P., Ledoux, C., Petitjean, P., & Srianand, R., 2008, *A&A*, 481, 327
- Noterdaeme, P., Petitjean, P., Carithers, W. C., et al., 2012b, *A&A*, 547, L1
- Nulsen, P. E. J., Barcons, X., & Fabian, A. C., 1998, *MNRAS*, 301, 168
- Ott, S., 2010, in *Astronomical Society of the Pacific Conference Series*, Vol. 434, *Astronomical Data Analysis Software and Systems XIX*, Mizumoto, Y., Morita, K.-I., & Ohishi, M., eds., p. 139
- Pearson, C., Lim, T., North, C., et al., 2014, *Experimental Astronomy*, 37, 175
- Péroux, C., Bouché, N., Kulkarni, V. P., York, D. G., & Vladilo, G., 2011, *MNRAS*, 410, 2237
- , 2012, *MNRAS*, 419, 3060
- Péroux, C., Kulkarni, V. P., Meiring, J., Ferlet, R., Khare, P., Lauroesch, J. T., Vladilo, G., & York, D. G., 2006, *A&A*, 450, 53
- Petitjean, P., Theodore, B., Smette, A., & Lespine, Y., 1996, *A&A*, 313, L25
- Pettini, M. & Pagel, B. E. J., 2004, *MNRAS*, 348, L59
- Pettini, M., Smith, L. J., King, D. L., & Hunstead, R. W., 1997, *ApJ*, 486, 665
- Popping, G., Caputi, K. I., Trager, S. C., et al., 2015, *MNRAS*, 454, 2258
- Prochaska, J. X., Chen, H.-W., Wolfe, A. M., Dessauges-Zavadsky, M., & Bloom, J. S., 2008, *ApJ*, 672, 59
- Prochaska, J. X., Gawiser, E., Wolfe, A. M., Castro, S., & Djorgovski, S. G., 2003, *ApJ*, 595, L9
- Prochaska, J. X., Herbert-Fort, S., & Wolfe, A. M., 2005, *ApJ*, 635, 123
- Prochaska, J. X. & Wolfe, A. M., 1997, *ApJ*, 487, 73
- Rafelski, M., Wolfe, A. M., Prochaska, J. X., Neeleman, M., & Mendez, A. J., 2012, *ApJ*, 755, 89
- Rao, S. M., Belfort-Mihalyi, M., Turnshek, D. A., Monier, E. M., Nestor, D. B., & Quider, A., 2011, *MNRAS*, 416, 1215
- Rao, S. M., Nestor, D. B., Turnshek, D. A., Lane, W. M., Monier, E. M., & Bergeron, J., 2003, *ApJ*, 595, 94
- Rao, S. M., Turnshek, D. A., & Nestor, D. B., 2006, *ApJ*, 636, 610
- Saintonge, A., Kauffmann, G., Kramer, C., et al., 2011, *MNRAS*, 415, 32
- Santini, P., Maiolino, R., Magnelli, B., et al., 2014, *A&A*, 562, A30
- Schaye, J., 2001, *ApJ*, 562, L95
- Schlafly, E. F. & Finkbeiner, D. P., 2011, *ApJ*, 737, 103
- Smith, H. E., Cohen, R. D., Burns, J. E., Moore, D. J., & Uchida, B. A., 1989, *ApJ*, 347, 87
- Srianand, R., Hussain, T., Noterdaeme, P., Petitjean, P., Krühler, T., Japelj, J., Pâris, I., & Kashikawa, N., 2016, *MNRAS*, 460, 634
- Steidel, C. C. & Hamilton, D., 1992, *AJ*, 104, 941
- Steidel, C. C., Rudie, G. C., Strom, A. L., et al., 2014, *ApJ*, 795, 165
- Storrie-Lombardi, L. J. & Wolfe, A. M., 2000, *ApJ*, 543, 552
- Straka, L. A., Johnson, S. D., York, D. G., Bowen, D. V., Florian, M., Kulkarni, V. P., Lundgren, B., & Péroux, C., 2015, *arxiv/1507.08047*; submitted to *MNRAS*
- Straka, L. A., Kulkarni, V. P., York, D. G., Woodgate, B. E., & Grady, C. A., 2010, *AJ*, 139, 1144
- Tacconi, L. J., Neri, R., Genzel, R., et al., 2013, *ApJ*, 768, 74
- Tiley, A. L., Bureau, M., Saintonge, A., Topal, S., Davis, T. A., & Torii, K., 2016, *MNRAS*, 461, 3494
- Tremonti, C. A., Heckman, T. M., Kauffmann, G., et al., 2004, *ApJ*, 613, 898
- Turnshek, D. A., Rao, S., Nestor, D., Lane, W., Monier, E., Bergeron, J., & Smette, A., 2001, *ApJ*, 553, 288
- Wang, W.-H., Kanekar, N., & Prochaska, J. X., 2015, *MNRAS*, 448, 2832
- Warren, S. J., Møller, P., Fall, S. M., & Jakobsen, P., 2001, *MNRAS*, 326, 759
- Weatherley, S. J., Warren, S. J., Møller, P., Fall, S. M., Fynbo, J. U., & Croom, S. M., 2005, *MNRAS*, 358, 985
- Weiß, A., Downes, D., Neri, R., Walter, F., Henkel, C., Wilner, D. J., Wagg, J., & Wiklind, T., 2007, *A&A*, 467, 955
- Wiklind, T. & Combes, F., 1994, *A&A*, 288, L41
- Wuyts, S., Förster Schreiber, N. M., van der Wel, A., et al., 2011, *ApJ*, 742, 96
- Zafar, T., Møller, P., Ledoux, C., et al., 2011, *A&A*, 532, A51

- Zafar, T., Møller, P., Péroux, C., Quiret, S., Fynbo, J. P. U.,
Ledoux, C., & Deharveng, J.-M., 2017, MNRAS, 465, 1613
Zwaan, M. A., van der Hulst, J. M., Briggs, F. H., Verheijen,
M. A. W., & Ryan-Weber, E. V., 2005, MNRAS, 364, 1467